Effects of interdiffusion on shear response of semi-coherent {111} interfaces in Ni/Cu

A. Selimov[1*], K. Chu[1], and D.L. McDowell[1,2]

[1]Department of Materials Science and Engineering, Georgia Institute of Technology, Atlanta, GA 30332, USA

[2]Woodruff School of Mechanical Engineering, Georgia Institute of Technology, Atlanta, GA 30332, USA

[*]Corresponding author, E-mail address: aselimov3@gatech.edu

Abstract

Intermixing of chemical species as a result of interdiffusion during the manufacturing of metallic nanolaminates leads to diffuse interface structures which have distinct properties compared to corresponding atomically sharp interfaces. The effect of interdiffusion-induced changes to the interface structure on interface shear strength is complex due to the presence of solute atoms and a reduced misfit dislocation density. The shear responses of {111} Cu/Ni nanolaminate interfaces with varying levels of interdiffusion are studied using atomistic methods to elucidate the effect of interface structure changes on shear deformation mechanisms. Models with diffuse interfaces exhibit improved interface shear strength relative to the atomically sharp case; however, shear strength does not increase monotonically with solute concentration. The distribution of maximum changes in energy per misfit node and non-uniform misfit node displacements, filtered using microrotation vector analysis, suggest heterogeneous interface resistance to sliding. No strong correlation is found between solute concentration near misfit node centroids and misfit node displacements, indicating the importance of the longer-range misfit dislocation structure. Increased activation of misfit dislocation glide is associated with larger solute concentrations as a result of increased misfit node displacements. Analysis of change in energy during the shear deformation process, however, reveals that interface sliding is dominated by the misfit node behavior. These findings highlight the importance of modeling realistic diffuse interface structures and emphasize the competing effects of solute concentration and interface misfit dislocation density.

1. Introduction

Nanolaminate metallic composites with high interface density exhibit mechanical properties that exceed those of each of the bulk constituent materials, e.g., improved yield strength, fatigue strength, radiation tolerance, and others [1–6]. These properties can be tailored by controlling layer thickness [7–10] and modulation ratio [11,12], or by adjusting interface characteristics such as misfit dislocation density [13–15]. The interfaces play a fundamental role in mechanisms that govern plasticity, e.g., defect nucleation [16,17], propagation of slip [18–20], and crack growth [21,22]. Computational studies can

efficiently evaluate an expansive parameter space at lower cost than experimental studies and can project prospective nanolaminate structure to realize improved material properties. It is important to strike a balance between approximations employed in such simulations and the associated idealization of the actual system or reduction in accuracy. For example, computational studies of nanolaminate materials commonly assume atomically sharp interfaces [23–26]. This assumption generally does not hold when constituent materials are miscible due to the interdiffusion of chemical species as a result of manufacturing processes [27-30]. These diffuse interfaces complicate interface structure and its evolution under applied loading; however, this additional aspect opens the possibility to further tailor mechanical responses. Cu/Ni nanolaminates manufactured through sputtering are one such system for which interdiffusion across the interface may occur [31] and the application of annealing heat treatments can lead to fine-grained layer composition control [32]. There is a need to characterize the effects of diffuse interfaces expected in manufactured nanolaminates to provide more realistic predictions of nanolaminate responses and to aid nanolaminate design.

Interfaces in nanolaminate materials can be broadly grouped into coherent, semi-coherent, or incoherent interfaces; these interact differently with lattice dislocations [33]. Semi-coherent interfaces form when both constituents have compatible crystal structures and layer thicknesses are above a material-specific critical value [34]. They are characterized by a network of misfit dislocations with spacing that depends on the lattice constant mismatch between constituent materials. These misfit dislocations resist slip transmission across the interface by reacting with incoming lattice dislocations [35,36]. The originating/terminating points for misfit dislocations, also referred to as misfit nodes, primarily contribute to the interface plasticity by serving as sites for generation of lattice dislocations [37] and sites for the initiation of interface sliding [38,39]. While the ideal atomically sharp semi-coherent interface between Cu/Ni has been well studied, the effects of interdiffusion on interface properties/evolution and the resulting impact on the overall nanolaminate properties has received little attention and motivates the present study.

Interdiffusion has two primary effects on semi-coherent interface structure. The first is the adjustment to the bulk layer lattice parameters, namely in terms of a lower misfit dislocation density than in the case of a sharp interface. Experimental x-ray diffraction studies have noted shifts in lattice parameter for nanolaminate layers with annealing and interdiffusion [40–42]. Misfit dislocation density is an important parameter; Yang et al. [15] found that the shear response of an interface is closely tied to the misfit dislocation density, i.e. a higher misfit dislocation density can increase the interface shear strength. Work by Xu et al. [36] showed that a higher misfit dislocation density was associated with a higher interface resistance to slip transmission. The reduction in misfit dislocation density is also accompanied by changes to the stacking fault energy of the interface which affects the size of interface stacking fault regions and the misfit dislocation core structures [43]. Increases in the stable stacking fault energy is shown to correlate with reduced interface shear strength for the Cu/Ag system [44]. The reduction in misfit between layers as a result of interdiffusion thus serves to reduce the shear strength of the interface.

The second effect of interdiffusion on the interface structure is the presence of solute atoms which serve as sites for dislocation generation or as pinning points for interface

misfit dislocations [44]. Generally, solutes impede dislocation motion by virtue of solute segregation to dislocation lines [45] or solute strengthening due to concentration fluctuations in a random alloy [46]. Molecular dynamics studies on the effects of Ni solutes on dislocation mobility in Cu/Ni solid solutions show that Ni solutes can impede dislocation glide, reducing effective dislocation velocities [47]. Local solute concentration fluctuations can lead to reduced energy barriers for the cross-slip of screw dislocations [48]. Dislocation generation from semi-coherent interfaces due to Friedel-Escaig-like cross-slip of misfit dislocations has been reported in the literature [39]. The presence of solute atoms therefore leads to increased interface shear strength. which acts in opposition to the reductions of interface shear strength associated with reduced misfit dislocation density as previously discussed. Whether interdiffusion leads to improvements in mechanical properties, or their deterioration, depends on which structural change, either increase in solute content or reduction in misfit density, has a greater impact on interface properties.

Atomistic simulations are required to determine the interplay between these two competing mechanisms and their effect on interface properties, given that the interaction between misfit density and solute effects alter pathways for atomic-scale restructuring of the interface that accommodates deformation. Some preliminary studies on the effects of alloying and interdiffusion on the properties of semi-coherent interfaces have been explored in the literature. Work by Gola et al. [49] found that alloying Cu layers with Ag in Cu/Ni bicrystals led to an increased resistance to both shear and slip transmission due to an increase in lattice mismatch and thus misfit dislocation density. Wang et al. [44] studied the misfit dislocation structure of Ag/Cu bicrystals after alloying each individual layer with the other species. They found a reduction in the yield stress as a result of increased alloying, a change in the site of dislocation generation from the misfit dislocation nodes to points of impingement between solute clusters and misfit dislocations, and an increase to the interface shear resistance due to solute pinning of misfit dislocations. In these previous approaches, relatively low solute concentrations were studied, differences in misfit dislocation density were limited, and alloying was admitted in only one of the two layers. Interdiffusion in Cu/Au bicrystals resulted in the development of a 3D dislocation structures at the diffuse interface distinct from the initial 2D semi-coherent interface misfit structure [50]; however mechanical behavior of these interfaces was not studied. Experimental studies on the properties of diffuse interfaces in the Cu/Nb system, with incoherent interfaces, show improved yield strength and ductility compared to the atomically sharp case [51,52]; however, similar studies on nanolaminates with semi-coherent interfaces are lacking. This motivates studies of bicrystal geometries with more realistic diffuse semi-coherent interfaces with different degrees of interdiffusion to quantify the combined effects of misfit dislocation density and solutes on interface properties.

The present work focuses on effects of interdiffusion on the interface misfit dislocation structure and interface shear response. Molecular dynamics (MD), molecular statics (MS), and Monte-Carlo (MC) methods are used to study the effects of solutes and decreased layer misfit on the properties of semi-coherent interfaces in the Cu/Ni system. Solute concentrations of up to 30% in each layer are studied. First, the methodology and geometries used to study the effects of interdiffusion induced interface structure on the

properties of the material are presented. Characterization of the interface structure and the solute distribution follows. Finally, the effects of solutes and modified misfit dislocation spacing on mechanical response in shear are discussed with a focus on interface sliding. This work highlights the importance of accounting for interdiffusion induced interface structures for modeling manufactured nanolaminate materials.

2. Methodology

2.1. Models and simulation approach

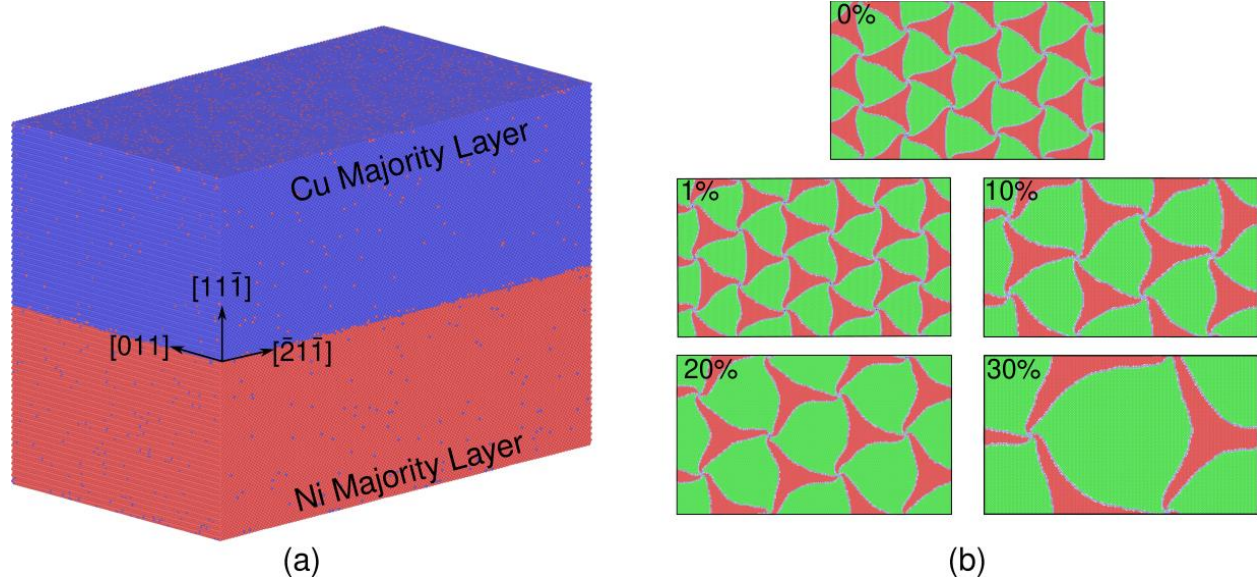(a)   (b)

Figure 1: a) Image of Cu/Ni nanolaminate model geometry with 1% solute concentration. All investigated geometries have the same orientations. b) Common neighbor analysis of the interface structure with overlaid misfit dislocation lines computed via the Dislocation Extraction Algorithm [53]; misfit dislocation density decreases with increasing solute concentration up to 30%.

A representative Cu/Ni model geometry investigated in this work is presented alongside the interface structures in Fig. 1. All models are generated using in-house codes. First, a rule of mixtures is used to calculate the changes in lattice parameters due to interdiffusion for each of the nanolaminate layers. Blocks of Cu/Ni solid solutions are then generated by creating pure blocks of Cu and Ni with the correct concentration dependent lattice parameter, given in Table 1. In this work, we investigate equal degrees of 0%, 1%, 10%, 20%, and 30% interdiffusion in both layers. The two blocks of Cu/Ni solid solutions are then combined with surface normal along the $[11\bar{1}]$ direction to form a semi-coherent interface. The solute distributions in each layer are initially random in this procedure; however, realistic solute concentrations are expected to be higher at interfaces following annealing [31].

Table 1: Parameters for geometries under investigation.

Layer Concentration	Lattice Constants	Dimensions	Number of Atoms	Misfit Spacing
Cu/Ni	3.615/3.524	51.2 x 29.6 x 36.9 nm	4,971,060	10.1 nm
$Cu_{.99}Ni_{.01}/Ni_{.99}Cu_{.01}$	3.615/3.524	51.2 x 29.6 x 36.9 nm	4,971,060	10.1 nm
$Cu_{.9}Ni_{.1}/Ni_{.9}Cu_{.1}$	3.606/3.533	42.7 x 24.7 x 36.9 nm	3,457,800	12.2 nm
$Cu_{.8}Ni_{.2}/Ni_{.8}Cu_{.2}$	3.597/3.542	57.2 x 33.0 x 36.9 nm	6,178,320	17.0 nm
$Cu_{.7}Ni_{.3}/Ni_{.7}Cu_{.3}$	3.588/3.551	43.0 x 24.8 x 36.9 nm	3,492,900	26.2 nm

A hybrid MC/MD scheme is employed for simulated annealing, executed using the LAMMPS simulation code [54]. The initial interface structure is minimized using sequential conjugate gradient energy minimization and FIRE [55] steps with increasing force tolerances. During the conjugate gradient steps, the strain energy of the system, calculated by the Parrinello and Rahman expression [56], is minimized using built in LAMMPS options. Following this rigorous structural relaxation, the hybrid MD/MC scheme is applied. First the system temperature is initialized to 700K by applying a scaled Gaussian velocity distribution and equilibrated using an NPT ensemble over 10 ps. Following the relaxation, an additional 100 ps of dynamics in an NPT ensemble is conducted. Every ten iterations, or 0.01 ps, two hundred MC swap attempts are executed. To maintain the target solute concentration in each layer, the swaps attempts are restricted to two atoms within the same layer. In total two million swaps are attempted, one million per layer. This is a relatively low number of swaps compared to the overall model size. Initial solute distributions therefore may not correspond to the fully energy minimized ones, specifically considering the extent of solute segregation that occurs to misfit dislocations. Analysis of model deformation, however, is not restricted only to the initial interface sliding. The effect of initial solute structure on subsequent interface sliding or yielding occurring after deformation of the misfit pattern away from the initial position should be reduced as the misfit pattern glides over regions of the interface with more random spatially distributed solutes. Overall interface solute concentration is expected to be more important, and the concentration profiles for the investigated geometries shown in Fig. 2b) exhibit increasing solute concentration near the interface as expected [32]. Convergence of the system energies with successful swaps can be determined by the change in energy per atom, as seen in Fig. 2a). Observed fluctuations in the energy arise from the thermostatting process. The change in energy per atom meets a tolerance of $1x10^{-6}$ eV/atom.
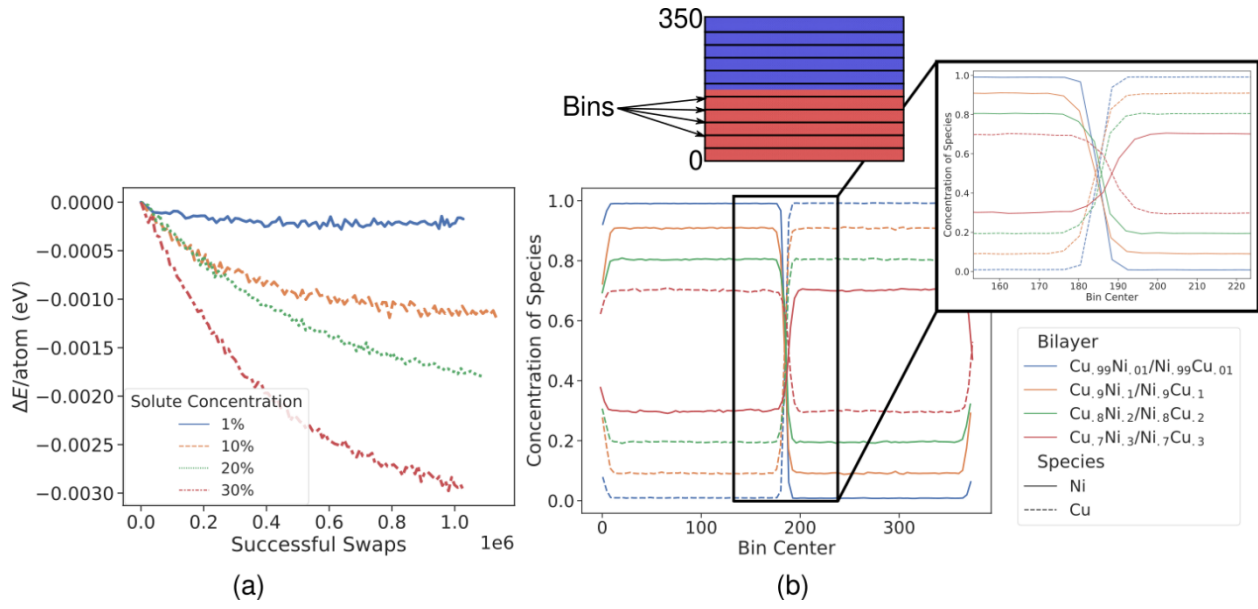
Figure 2: a) Change in per atom energy versus successful swaps. Fluctuations occur as a result of the thermostatting applied. b) Concentration profiles for all models with diffuse interfaces. As expected, solute concentrations near the interface are higher than in the bulk.

Periodic boundaries are used in all dimensions, approximating an infinite nanolaminate system with some constraint imparted by the periodic boundaries. As such, the length of the simulation cell must be set to a value which is a multiple of the lattice repeat distance for both layers. Any change in lattice constant due to interdiffusion leads to a different lattice repeat distance; thus, the model dimensions differ for each solute concentration. Efforts were taken to select the most similar dimensions, but variation in both in-plane dimensions is noted. This work utilizes the Onat and Durukanoğlu Cu/Ni potential [57] due to their focus on fitting the Cu-Ni interaction term leading to improved accuracy of calculated mixing enthalpies compared to other EAM potentials. This potential also accurately fits stable and unstable stacking fault energies for bulk Cu and Ni validating its use for modeling mechanical response in the present work. It is also noted that because the lattice mismatch between Cu and Ni is small, the differences in the lattice constants between the different alloys studied is also small. As a result, although the solute misfit volume is not constant between the different investigated geometries, the differences are small enough to be considered negligible. In systems where the lattice constant mismatch is large this may not necessarily hold and the dependence of solute strength, through the atomic misfit volume, on the layer solute concentration may need to be considered. Models are analyzed using OVITO [58] and its Dislocation Extraction Algorithm (DXA) [53] is used to determine positions and Burgers vectors of interface misfit dislocations. The contribution of the potential to the virial stress [59] is used to calculate the stress for these models and is referred to as the interatomic potential stress for clarity

We investigate the shear properties of the system using standard MS strain-controlled loading approaches [60]. The annealed models from the above hybrid MC/MD results are assessed. First, it is necessary to employ shrink-wrapped boundaries in the z-[11$\bar{1}$] dimension, while the in-plane dimensions remain periodic. Two full atomic layers in both

the top and bottom z-dimension are held fixed by setting all components of the force vector to 0 at each step. An incremental shear strain γ_{zx} or γ_{zy} shear strain with a step size of 2.5×10^{-5} is then applied to the cell by displacing all atoms in the fixed upper layer by a vector dx according to the target strain from 0 initial strain in all cases, computed simply as $dx = \gamma_{xz}L_z$, where L_z is the length of the cell in the z-dimension. The system energy is then rigorously minimized through the sequential conjugate gradient/FIRE approach as above. Conjugate gradient minimization to an energy tolerance of 1×10^{-12} with box relaxation is first applied with box relaxation to target pressure of 0 bar in the in-plane dimensions, followed immediately by FIRE energy minimization to a tolerance of 1×10^{-12}. Total system shear stress of the minimized system at each strain increment is determined by summing the potential contribution to virial stress in the strain direction τ_{zx} or τ_{zy}. The next fixed shear strain increment is then again applied via per-atom displacement, and the process repeats up to total shear strain of 2.0×10^{-2}.

2.2. Microrotation vector analysis of interface deformation

In addition to conventional metrics for analysis of atomistic models, such as Common Neighbor Analysis (CNA) [61], the microrotation vector is also used to reveal in more detail the interface deformation. The microrotation vector is defined as [62,63]

$$\phi_k = -\frac{1}{2}\varepsilon_{ijk}\left(R_{\text{skew}}\right)_{ij} \tag{1}$$

Where ε is the permutation symbol and R_{skew} is the skew symmetric part of the rotation tensor $\textbf{\textit{R}}$ in the right polar decomposition of the deformation gradient $\textbf{\textit{F}}$, i.e.,

$$\textbf{F} = \textbf{RU} \tag{2}$$

where $\textbf{\textit{U}}$ is the right stretch tensor. Analysis of the atomic microrotation vector has been previously applied to the Cu/Ni semi-coherent interface [38] to elucidate both magnitudes and directions of atomic restructuring associated with interface sliding. Components of the microrotation vector describe the rotation of lattice vectors attributed to deformation such as dislocation glide, stacking fault restructuring, grain boundary sliding, and the glide of interface misfit dislocations. Microrotation vector magnitudes reflect the degree of restructuring with characteristic values or ranges quantified for a variety of deformation processes such as dislocation glide and grain boundary migration [62]. The interested reader is referred to Tucker et al. [63] for more in-depth description of the microrotation vector and its calculation.
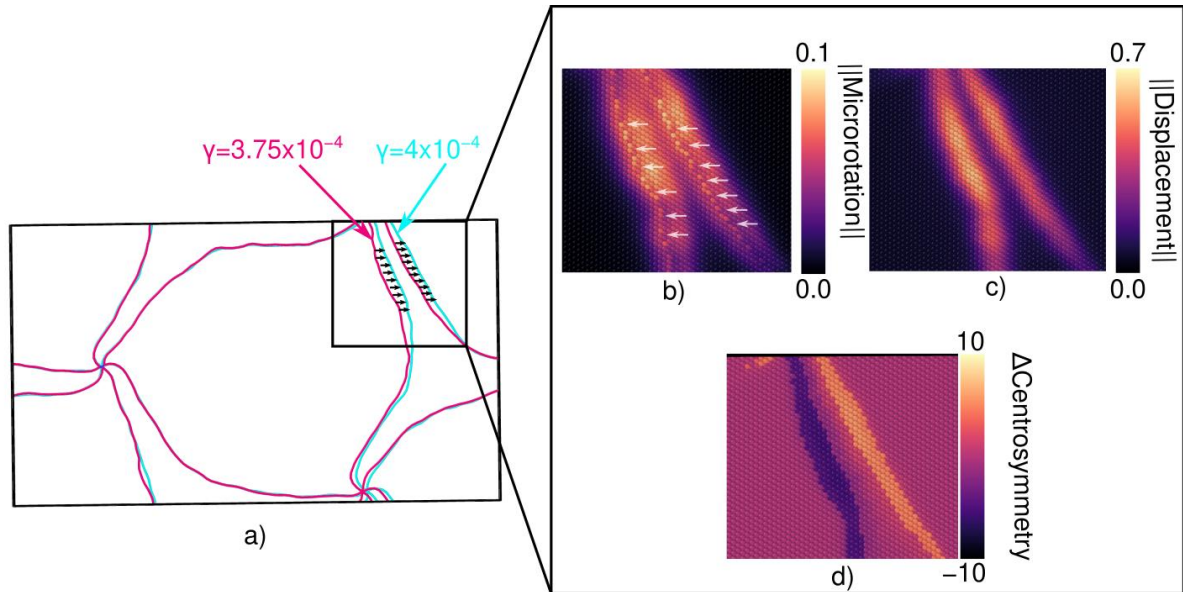
Figure 3: a) Change in the interface misfit dislocation pattern for the 30% solute concentration model as a result of applied shear strain to two different levels. b) Increased microrotation vector magnitude is associated with the structure change that results from the glide of interface misfit dislocations with higher magnitude indicating more complex structure changes. Starting dislocation lines can be clearly observed as lines of lower microrotation as highlighted by the white arrows. c) The displacement magnitude distribution does not reveal dislocation lines and instead exhibits a smooth distribution while d) the change in centrosymmetry distribution does not capture longer range deformation fields generated to accommodate the localized structure change.

The microrotation vector, atomic displacement vector, and change in centrosymmetry are compared in Fig. 3 as metrics to analyze the evolution of the interface misfit dislocation pattern after shearing for the 30% solute concentration model. The displacement vector magnitude is distributed smoothly as observed in Fig. 3c) complicating the demarcation of regions that have undergone structure change. This is because affine deformation of the atomic structure affects the value of the displacement vector and because the displacement vector does not consider the local atomic structure. The change in centrosymmetry parameter, Fig. 3d), can capture changes to atomic crystal structure well but does not capture the longer-range deformation fields associated with the local structure changes. The microrotation vector distribution in Fig. 3b) more effectively reflects the transformation of the underlying atomic structure compared to the other metrics. For example, the lines of atoms with lower microrotation vector magnitudes visible in Fig. 3b) correspond to those originally within the dislocation core. The lower microrotation vector magnitude for these atoms reflects the lesser rotation to underlying lattice vectors necessary for the transformation from the intermediate dislocation core structure to either the fcc or hcp crystal structure. This is compared to the rotation necessary for the full transformation from fcc to hcp or vice-versa. The position of the dislocation in the final structure corresponds to atoms with a lower microrotation vector magnitude as well. Regions bound by these two lines of lower microrotation vector magnitudes correspond to

those which have undergone the full transformation from fcc to hcp or vice-versa and can be extracted by filtering atomic microrotation vector magnitudes. Longer range deformation fields required to accommodate glide induced structure change are also captured and can be analyzed if desired. The microrotation vector thus serves as a powerful tool for analyzing the interface deformation.

2.3. Excess volume analysis for tracking node positions

It is necessary to track misfit node displacement to quantify relative interface motion. Misfit node displacement can then be considered to understand the differences in interface sliding mechanisms among various interfaces. For this purpose, excess volume analysis, as originally presented by Shao et al. [37], is combined with a K-Means clustering algorithm [64] to determine the centroids of excess volume regions associated with misfit nodes. This method is performed on single atomic layers and can be used to analyze the excess volume on either the Cu or Ni majority side of the interface. The present work uses the single layer of atoms on the Cu majority side of the interface to select misfit node centroid positions due to the larger fluctuations in excess volume magnitude which makes selection of proper filter values simpler. Analysis of the Ni majority side of the interface leads to equivalent misfit node centroid displacements. The excess volume analysis uses a Delaunay triangulation as implemented by the Scipy library [65], shown in Fig. 4, where the area of the triangle in the current mesh is compared to the area of the triangle in bulk. The area associated with the alloy in bulk (A^0) can be calculated using

$$A^0 = \frac{\sqrt{3}}{4} b_{\text{perfect}}^2 \tag{3}$$

where the ideal Burgers vector (b_{perfect}) is calculated from the solute concentration dependent bulk lattice constants, as shown in Table 1. The area of a triangle in bulk is subtracted from the area of the triangle in the current configuration and then multiplied by the height of the atomic layer (h), i.e.,

$$\Delta V = h \left(A - A^0 \right) \tag{4}$$

where A is the area of a triangle in the current configuration. This results in a distribution of excess volume across the mesh, such as in Fig. 4b). To determine the misfit node position, triangles with excess volumes below 0.2 Å^3 are removed. The centroid of the remaining triangles, which form clear groups at the misfit nodes as shown in Fig. 4c), are then clustered using a K-Means clustering algorithm. The centroids of these clusters correspond to misfit node centroid position and can be tracked with applied loading.
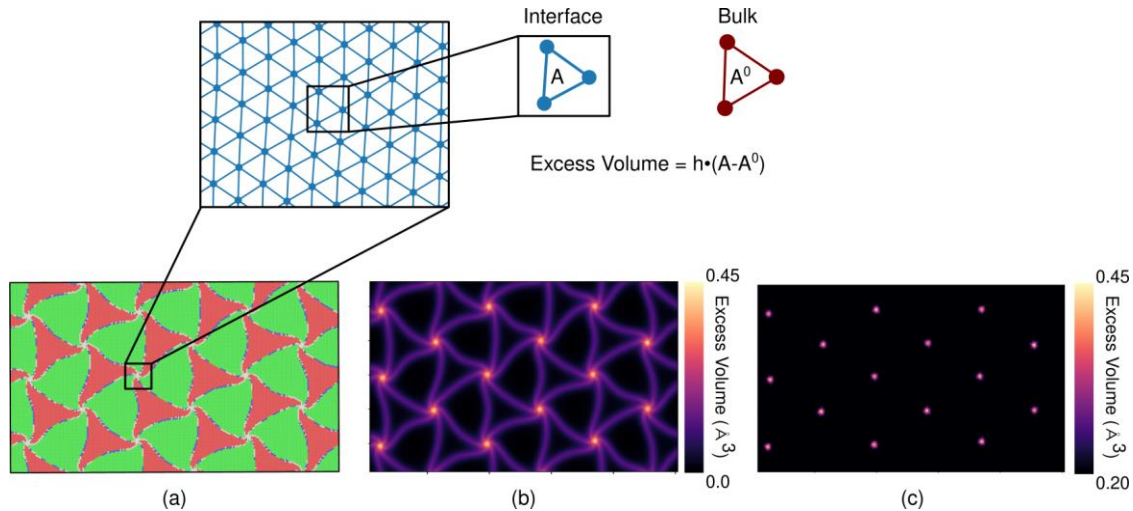
Figure 4: Summary of misfit node cen\troid calculation using excess volume analysis. a) Representative interface structure with atoms colored by CNA with green atoms in an fcc structure, red atoms in an hcp structure, blue atoms in a bcc structure, and white atoms in an undefined structure. The inset image shows the Delaunay triangulation used to calculate excess volume. b) Excess volume plot of the Cu side of the interface for the 0% solute concentration model. Misfit dislocations and misfit dislocation nodes have high excess volume compared to fcc and hcp regions of the interface. c) Interface excess volume map filtered to extract misfit node centroid positions.

3. Results and Discussion

3.1. Effects of interdiffusion on misfit dislocation structures at semi-coherent interfaces.

All interface structures presented in Fig. 1b) exhibit the well-established spiral pattern associated with the Cu/Ni semi-coherent interface [66]. In Fig. 5, the unrelaxed and relaxed interface structures are shown for both the 0% and 20% solute concentration models in more detail. Dislocation lines in addition to Burgers vector, line sense, and character are analyzed using the DXA algorithm [53]. In Fig. 5c) it is observed that the dislocation Burgers vectors and line senses match for both models. The pattern of the atomic displacement field as a result of interface relaxation also matches very closely. Dislocation character, calculated via DXA, is reflected as the color of the dislocation line. Misfit dislocations have predominantly edge character as indicated by the majority blue line color. Models with higher solute concentrations, however, have increased mixed character, denoted by a light blue or white color, as a result of increased dislocation line curvature. The increase in the dislocation line length is compensated for by the reduction in self-energy as discussed in the literature [43]. This analysis shows similar misfit dislocation patterns for all investigated geometries. It is also noted that the shear induced interface sliding discussed in following sections results in the translation of the misfit dislocation network without any dislocation reactions. Misfit dislocation Burgers vectors and character are generally conserved from the initial configuration, e.g., Fig. 5. As a result, the

comparison of interface energetics for sequential interface sliding events is valid. This type of shear sliding behavior is characteristic of semi-coherent metal/metal interfaces [15, 39] and has been observed for metal/ceramic interfaces as well [67]. The interested reader is referred to Dodaran et al. [68] for more in-depth analysis of the Cu/Ni semi-coherent interface.
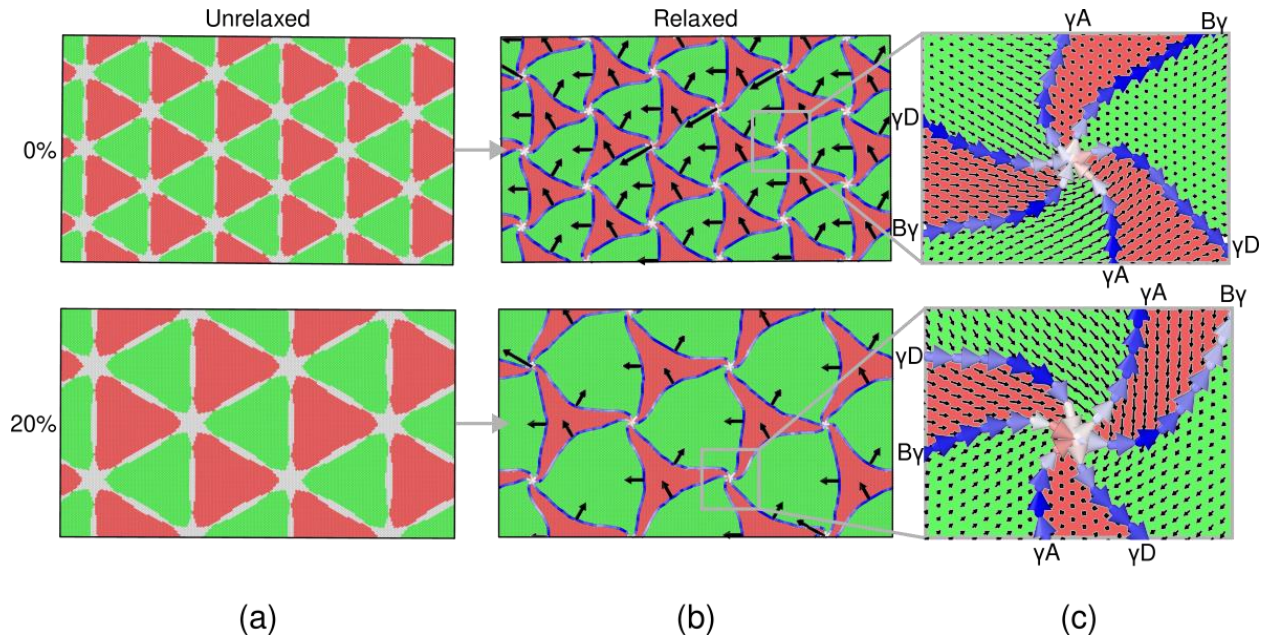

Figure 5: (a) Unrelaxed interface structure with atoms colored by Common Neighbor Analysis. Red atoms are in an HCP structure, green atoms are in an FCC structure, and gray atoms are in other structures. (b) Relaxed interface structure with blue lines denoting the dislocations as calculated via DXA and black arrows denoting the Burgers vectors of the dislocation. (c) Zoom in on a single misfit dislocation node with dislocation line sense visualized as the blue arrows and dislocation Burgers vectors labeled. Black arrows indicate directions of atomic displacements between unrelaxed and relaxed configurations.

While interdiffusion does not cause significant changes to misfit dislocation Burgers vectors or character, outside of slightly increased mixed character, it is expected to impact the stacking fault energy of the interface. However, characterization of these changes to interface stacking fault energy is not straightforward. Yao et al. [69] developed a Peierls-Nabarro model for interfacial misfit dislocation arrays in which one of the necessary parameters was the generalized stacking fault energy of the interface. For this they used the generalized stacking fault energy of the relative coherent interface, generated by using the average lattice parameter for both constituents. For the geometries studied in this work, the relative coherent interfaces would have identical lattice parameters and as such would isolate primarily the effects of solute atoms on the interface stacking fault energy as opposed to the reduced misfit. Shao et al. [43] studied the generalized stacking fault energy in more detail comparing various model geometries which all exhibited slightly different unstable and stable stacking fault energies. Because the present work is concerned primarily with the role that interdiffusion plays on the evolution of the interface structure

and the stacking fault energy is not required as a parameter for the presented analysis, such in-depth characterization is considered outside its. The trends for stacking fault energy, however, can be understood from analysis of the mean excess energy contained in the FCC and intrinsic stacking fault (ISF) regions and the percentage of atoms in the ISF structure.
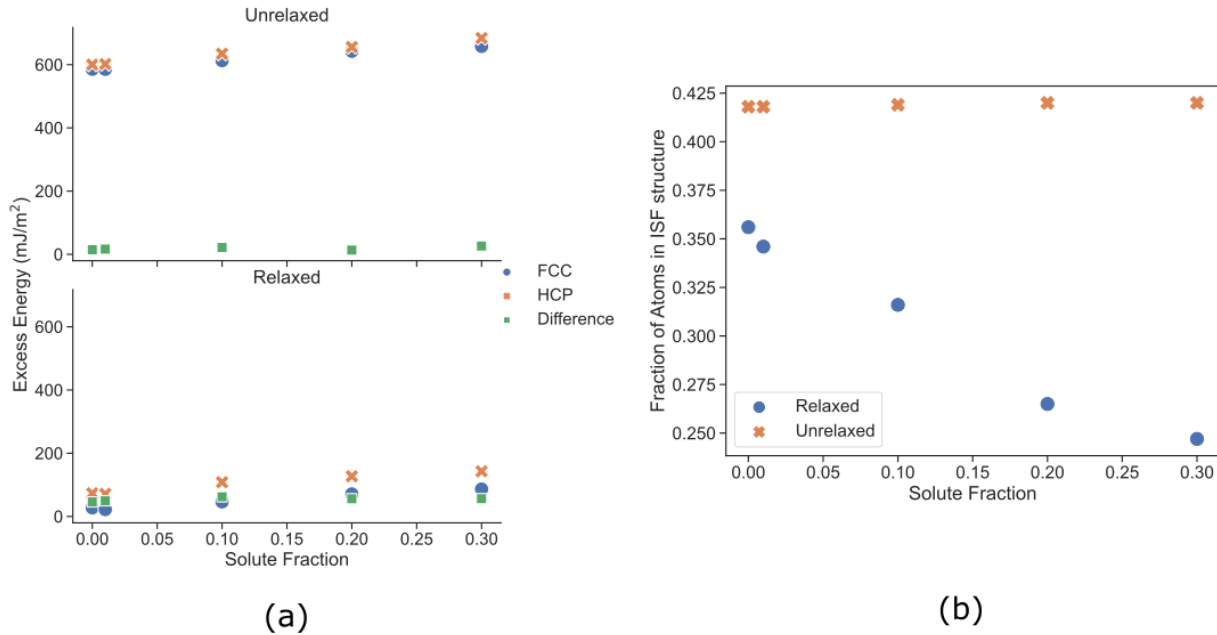

Figure 6: (a) Excess energy per unit area for FCC and ISF regions in addition to their difference at each solute fraction. (b) Fraction of interface atoms in ISF structure versus model solute fraction. A near-linear reduction in the fraction of ISF atoms is observed with increasing solute fraction. This is in contrast to the difference in the FCC and ISF energies which shows no clear correlation with solute fraction.

In Fig. 6a) it is observed that the total energy difference per unit area for FCC and ISF structures is small for the unrelaxed models and increases slightly after the hybrid MC/MD annealing and energy minimization. The individual energies of both FCC and ISF regions exhibit a positive correlation with the solute fraction before and after the relaxation procedure. This increase in the energy of both FCC and ISF regions can be attributed to both the presence of solute atoms at the interface and the additional strain associated with the concentration-dependent lattice parameters. The minimum and maximum energy differences between FCC and ISF regions post relaxation are 45 mJ/mm^2 and 62 mJ/mm^2 for the 0% and 10% solute concentration models, respectively. Neither before nor after the relaxation procedure, does the energy difference show a clear trend with solute fraction. This is in contrast to the fraction of atoms in the ISF structure which exhibits a clear negative correlation with the solute fraction of the models, indicating increasing contraction of ISF regions with increasing solute fraction. The difference in the size of the interface ISF regions post relaxation cannot be attributed to differences in the interface

geometry as the area fractions of the interface belonging to ISF regions are equal prior to relaxation. These factors suggest that the reduction in the area of ISF regions, and the associated increase in the misfit dislocation line curvature, results primarily from the reduction in the misfit dislocation line self-energy associated with changing from pure edge to mixed character as opposed to a large difference in the stacking fault energy with increasing solute fraction. Longer misfit dislocation lines, associated with increased solute fractions, exhibit increased curvature as measured by the decrease in the area fraction of ISF regions of the interface. More in-depth analysis of the interface stacking fault energy is necessary to validate this conclusion and is left to future work.

3.2. Investigation of solute clustering and solute segregation at the Cu/Ni interface

Partial radial distribution functions calculated for all concentrations are presented in Fig. 5. These partial radial distribution functions are calculated only for interface atoms and show that the hybrid MC/MD procedure generally leads to increased intermixing of chemical species. Clustering is not promoted by the annealing process for the investigated geometries. Additionally, it is expected that solutes will segregate to misfit dislocations at the interface due to the associated excess volume. To characterize this segregation, the Dislocation Extraction Algorithm (DXA) [53] is utilized to determine points along the misfit dislocation lines. Interface atoms within a radius of 1.5 nm of these points are then determined and the fraction of those atoms which are solutes are calculated. This process is repeated for interface atoms near misfit dislocation nodes. Kernel density estimation is used to approximate the distribution of the solute atom fraction for all sampled points along the misfit dislocation lines.
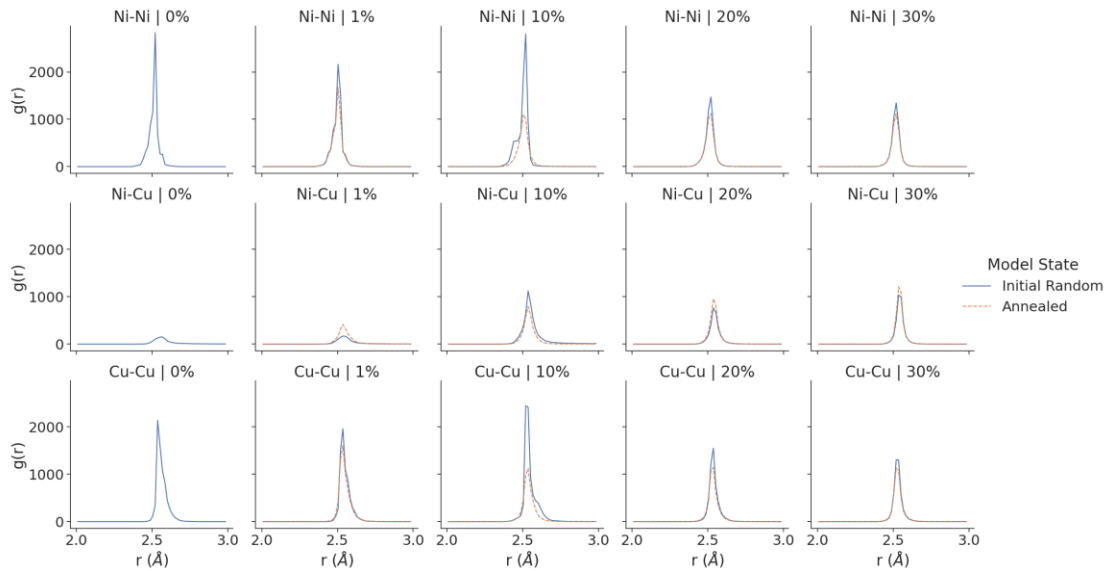

Figure 7: Partial radial distribution functions for investigated concentrations before and after the hybrid MC/MD annealing for atoms within one atomic layer on either side of the interface. Clustering of Ni or Cu is not observed as seen by the increases to the Ni-Cu partial radial distribution function and decreases to Cu-Cu and Ni-Ni partial radial distribution functions.

The fraction of solute atoms near misfit dislocation lines or misfit dislocation nodes specifically are compared to the overall interface solute fraction in Fig. 6. It is observed that the atomic neighborhoods near misfit dislocations have higher solute fractions than the overall interface. This confirms solute segregation to misfit dislocation lines. The misfit dislocation nodes and misfit dislocation lines both have similar fractions of solute atoms in surrounding atomic neighborhoods. The low standard deviation of the distribution for the 30% solute concentration annealed model is attributed to the reduced misfit node density within the geometry. The standard deviation for post-anneal solute fractions calculated for points along the misfit dislocation lines is approximately 0.02 for the 1% solute concentration model and 0.03 for the other solute concentrations. This non-uniform solute segregation is expected to lead to a distribution of energy barriers for misfit dislocation glide as solute drag forces [70] increase with increasing solute concentration as does the extent of pinning by solute configurations [71]. This is discussed in more detail in following sections on shear response of the models.
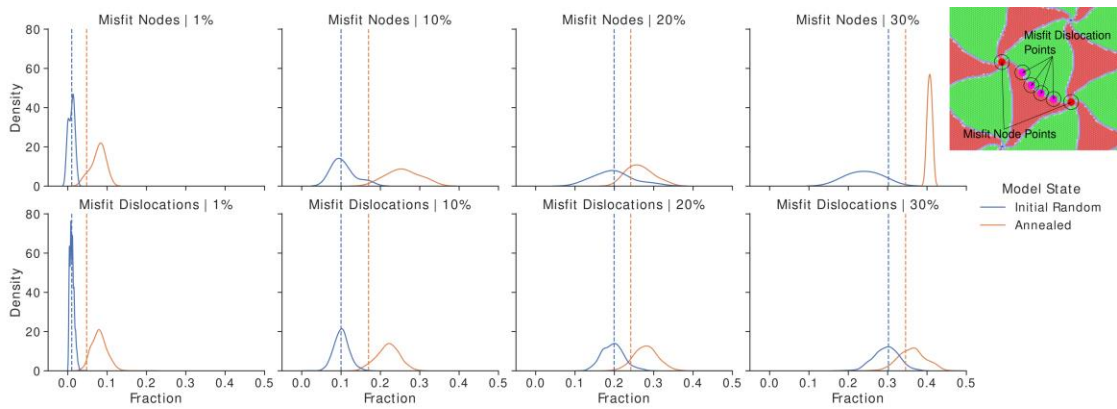

Figure 8: Kernel density estimate of the fraction of solute atoms within a radius of 1.5 nm of points sampled from the misfit dislocation line and the misfit dislocation node positions. Dashed vertical lines represent the overall interface solute fraction. Significant solute segregation to both misfit dislocations and misfit nodes are observed. Solutes have only a small preference for misfit nodes over misfit dislocations. The inset figure is a schematic highlighting points used to generate misfit dislocation distribution and misfit node distribution.

3.3. Effect of solute concentration on interface shear strength and misfit node glide

Stress-strain curves for the investigated geometries under shear loading are presented in Fig. 7a-b). The presence of solutes increases the interface shear strength and resistance to sliding relative to the atomically sharp interface case (0%), as observed by the increase in the average stress maxima in Fig. 7c). The increase in shear strength between the models with 0% solute and 1% solute can be attributed solely to the effects of the solutes since the interface misfit densities are essentially identical. Further increases to solute concentration do not result in a clear trend for average nor median stress maxima values. This may be

attributed to the competing effects of increased solute concentration, which improves interface shear strength [44], and the reduced misfit density, which reduces shear strength [15]. The spread of stress maxima values also increases, with the 30% model having the largest spread of approximately 0.07 GPa. The spread of stress maxima values is a result of heterogeneous solute configurations encountered by the misfit dislocation pattern as interface sliding occurs. These locally fluctuating solute configurations offer different resistance to misfit dislocation glide and non-uniform strengthening. The various solute configurations encountered may also result in the lower minimum stress values observed for the models with solutes present compared to the 0% solute concentration model. As the misfit dislocations overcome solute configurations with higher resistance to interface sliding, a significant amount of stress is relaxed as the misfit pattern glides over regions of the interface with lower resistance to sliding. The period of the oscillations observed in Fig. 7a-b) strongly indicates that interface sliding does not occur uniformly. In the case of the 0% solute concentration model, the stress builds up to the maximum value and is relaxed to a minimum value over very few strain steps. In the presence of solutes, the stress build-up and relaxation occur gradually which can be explained by the non-uniform glide of the misfit dislocations until they encounter solute configurations which have high resistance to glide. Use of a statistically sampled interface shear strength in reduced-order models, as opposed to an average interface shear strength, more accurately considers the underlying random distribution of solutes at the interface and may lead to improved predictions of real nanolaminate response. Alternative descriptions of the shear strength may be necessary for systems which form ordered patterns of solute clusters at the interface.
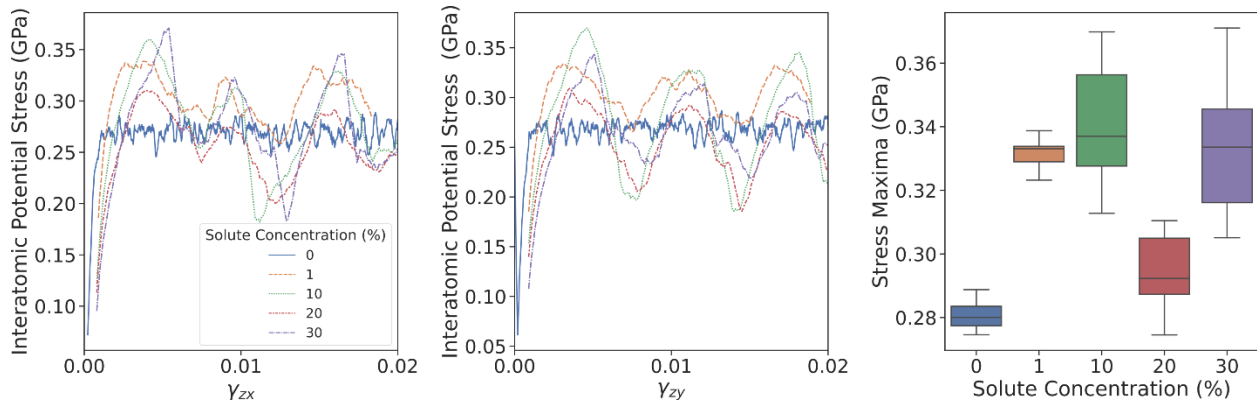

Figure 9: Shear stress-strain response of the entire model for the different geometries under investigation under a) zx shear and b) zy shear. c) shows the distribution of shear stress maxima in both directions for the different geometries. Increased maximum stress values indicate solute strengthening of the interface.

It is possible to track the misfit node displacements via excess volume analysis to determine the connection between the solute concentration dependent interface structures and the pathways for interface sliding. For this purpose, several simulation snapshots of the atomic structures are analyzed. Each snapshot is separated by a 2.5×10^{-4} shear strain increment. The displacement of misfit nodes between snapshots is computed by relating the misfit node centroid positions in the current snapshot to their positions in the previous

snapshot. This is performed for all models under investigation and is presented in Fig. 8. The 0% solute concentration sharp interface model exhibits uniform misfit node displacement for each strain increment, indicative of uniform interface sliding. This is not the case for the diffuse interface models with solutes. Addition of solutes is observed to increase the spread of node displacements, indicating that for any given strain step, only a subset of the misfit dislocation nodes accommodates the imposed strain through glide. This again suggests non-uniform resistance to misfit node glide and heterogeneous interface sliding. The increased node displacement with larger solute concentrations may result from one of two causes. First, glide of misfit dislocation nodes may be facilitated by increase of solute concentration, resulting in larger displacements per strain increment. Alternatively, local solute configurations may lead to significant variation in the interface resistance to misfit node glide, resulting in larger node displacements that overcome these regions of locally increased resistance. Both mechanisms are likely contributing factors as the increases in node displacements between the 0% and 10% solute concentration models correspond to an elevation of shear strength, while the increase between the 10% and 20% solute concentration models corresponds to a reduction. Analysis of energy changes associated with interface sliding in the following sections will discuss this in more detail.
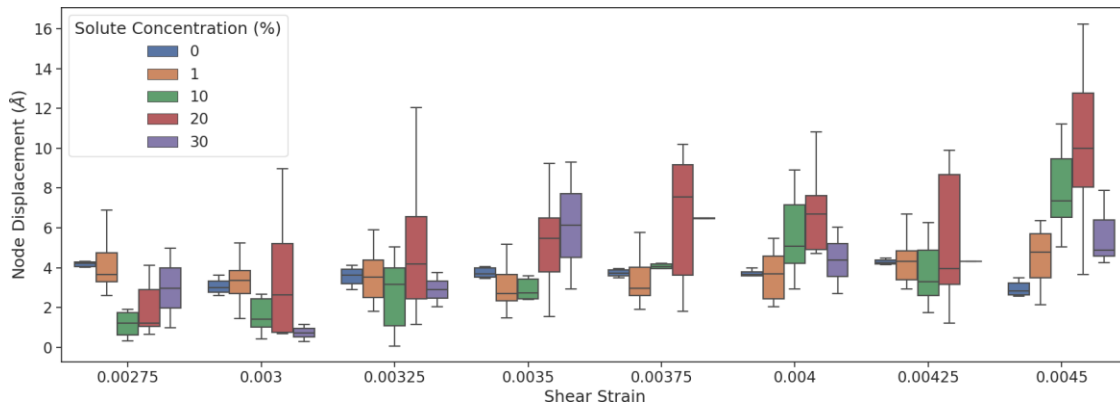

Figure 10: Range of misfit node displacements resulting from the application of sequential 2.5x10^-4 shear strain increments for all solute concentration models. The node displacement at each strain is calculated relative to the immediately preceding strain step, e.g. $\Delta x(\gamma=0.003)=x(\gamma=0.003)-x(\gamma=0.00275)$ *where x is the position of a single misfit node centroid and γ is the shear strain. The increased spread of node displacement values suggests distributed resistance to misfit dislocation glide along the interface. The 0% sharp interface exhibits very uniform misfit node displacements for all strain increments considered.*

3.4. Microrotation vector analysis of interface deformation and activation of misfit dislocation glide

Examples of interface atom microrotation maps are shown in Fig. 9 for all geometries subject to a shear strain high enough to deform the interface misfit dislocation pattern. A few observations can be made for the cases presented. First, the 0% solute concentration model exhibits a uniform distribution of atomic microrotation magnitudes, consistent with the results of the misfit node displacement analysis in the previous section. Maximum

values are noted at the misfit nodes accompanied by regions of lower microrotation values near misfit dislocation lines. In contrast, diffuse solute interface structures manifest a heterogeneous distribution of microrotation values, with atoms near certain misfit nodes and misfit dislocations exhibiting large microrotation magnitudes while atoms near other nodes with microrotation magnitudes close to zero. This further supports heterogenous resistance to misfit dislocation glide due to fluctuations in local misfit dislocation/solute configurations. The effect of local solute content on dislocation glide resistance will be discussed later. The second main observation is that the magnitude of the microrotation vector increases with the presence of solutes. This is qualified by the brighter regions near misfit nodes for all diffuse interface models and suggests that increased atomic restructuring accompanies interface sliding in those models.
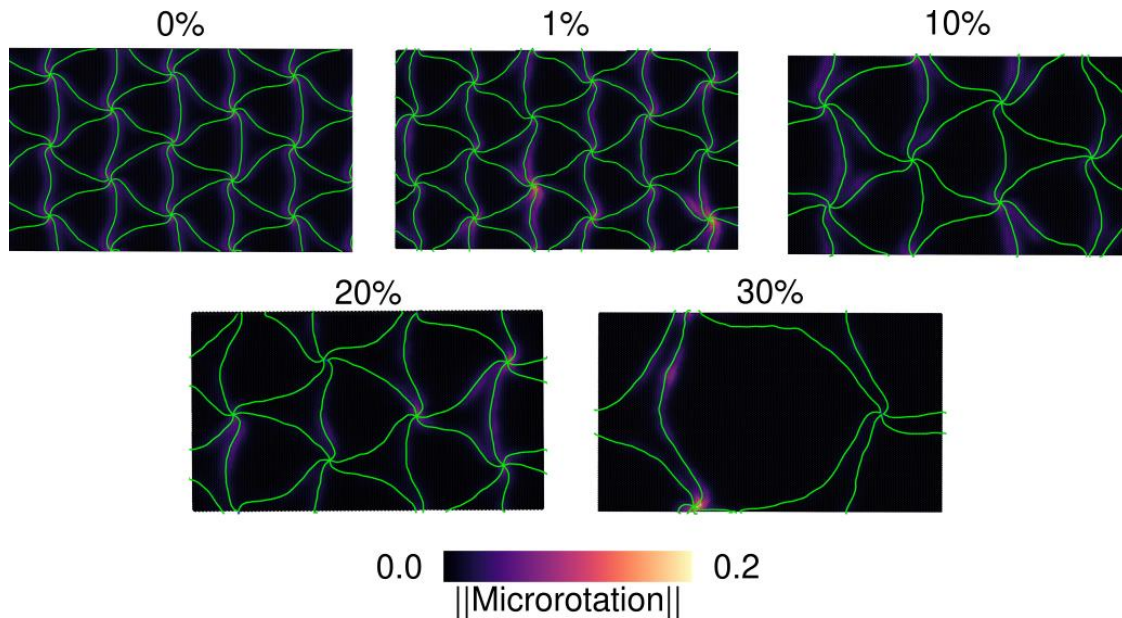

Figure 11: Interface microrotation maps for all solute concentrations subjected to a shear strain step which causes deformation of the interface misfit pattern. It is observed that the 0% solute concentration model exhibits a homogeneous microrotation distribution for atoms near misfit dislocations and misfit nodes resulting from uniform glide of the misfit dislocations. Models with solutes exhibit non-uniform distribution of microrotation values near misfit dislocations and nodes. This suggests non-uniform energy barriers resulting from the differing local solute environment which leads to glide of only portions of the interface misfit dislocations at any specified shear strain step.

The microrotation vector distribution is further quantified over several strain steps to characterize factors such as the degree of uniformity for interface sliding or degrees of atomic restructuring associated with interface sliding with relation to the overall solute concentration. The relationship between the microrotation vector magnitudes for atoms at misfit nodes and the interface deformation is visualized. This is done by selecting atoms with microrotation vector magnitudes greater than 0.06 and grouping them together using a K-Means clustering algorithm. Each cluster of atoms can then be assigned to a specific node by finding the minimum distance, as measured by the Euclidean norm, between the

atom cluster and the misfit node centroid calculated via the previously described excess volume analysis. These clusters of deformed atoms are only mapped if their centroids differ by at most the node displacement to ensure that only atoms participating in misfit node glide are isolated. The filter value of 0.06, slightly less than 0.07 which has been shown in the literature to correspond to full dislocation glide [63], is selected as it is the minimum cutoff to cleanly isolate misfit nodes that have undergone glide as measured by the excess volume analysis. That it is slightly less than the value for full dislocation glide suggests that certain atoms at misfit dislocation nodes do not fully transition between distinct atomic structures. This is likely the case for an atom that remains within the region of high atomic structure distortion, resulting from the strain fields associated with misfit nodes, before and after the misfit node displacement.

The relationship between both the mean and sum of the microrotation vector magnitudes for atoms deformed during misfit node glide are shown in Fig. 10. The mean atomic microrotation vector magnitude at a node and its displacement exhibits a clear positive correlation. Smaller node displacements lead to smaller swept areas and atoms at the glide front may end up in the misfit node core, undergoing only a portion of the atomic structure change associated with interface sliding. Larger misfit node displacements ensure that a greater portion of atoms involved undergo the full structure change. Larger means can also indicate more complex restructuring at the misfit node associated with the larger displacements. This may be the case when large local resistance to interface sliding requires more complex deformation of the local atomic structure to accommodate misfit node glide. The summed microrotation vector magnitude presented in Fig. 10 is related to the number of atoms participating in the deformation process. Atomic microrotation vector magnitudes associated with misfit dislocation/node glide take values of approximately 0.06~0.15. An increase in the summed microrotation from ~10 to ~100 requires a tenfold increase in the number of atoms participating in the deformation. The present analysis also shows that the 20% solute concentration model tends to exhibit more significant microrotation as a function of node displacement. The relationship between the increased microrotation vector magnitude near misfit nodes and the reduced shear strength compared to the other models with solute content will be discussed in more detail in the following section. These results tie the microrotation vector magnitudes to the underlying interface evolution, specifically the extent of misfit node glide. Microrotation vector analysis of atoms near misfit dislocation lines similarly shows the extent of misfit dislocation glide and can be used to quantify the activity of both misfit dislocation glide and misfit node glide.
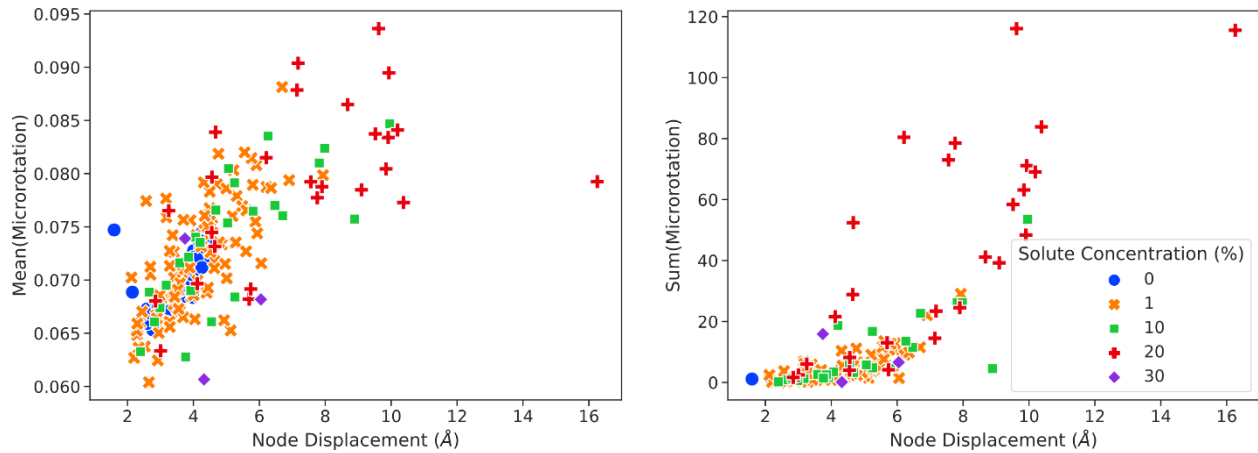
Figure 12: (a) Mean and (b) sum of microrotation vector magnitudes for atoms which have undergone deformation due to the glide of misfit nodes versus the displacement of that node. Larger node displacements are associated with both larger microrotation vector magnitude sums and averages. The increase of average misfit node microrotation with node displacement suggests more complex atomic structure deformation with larger misfit node displacements, while the increased sum of average misfit node microrotation with larger misfit node displacements is associated with the participation of larger numbers of atoms in the misfit node glide compared to smaller node displacements.

While there is a clear relationship between the microrotation at a node and its displacement, a large spread in values is still observed. Analysis of the solute fractions for atoms which are deformed by the glide of a misfit node can provide insight into the influence of local solute environment on either the spread in the misfit node displacements observed or the spread in the microrotation values for a given node displacement. As shown in Fig. 11, the local solute environment does not correlate strongly with either the average node microrotation or the node displacement. This suggests that local misfit node glide is not primarily dependent on the local solute environment and is instead highly coupled to the glide of the entire misfit pattern. The configuration formed by the overall misfit pattern and the distributed solute atoms likely exhibits improved correlation with resistance to sliding. Characterization of these configurations through more complex atomic structure analysis such as the smooth overlap of atomic positions (SOAP) metric [72] may provide insight into the structural factors which lead to improved sliding resistance.
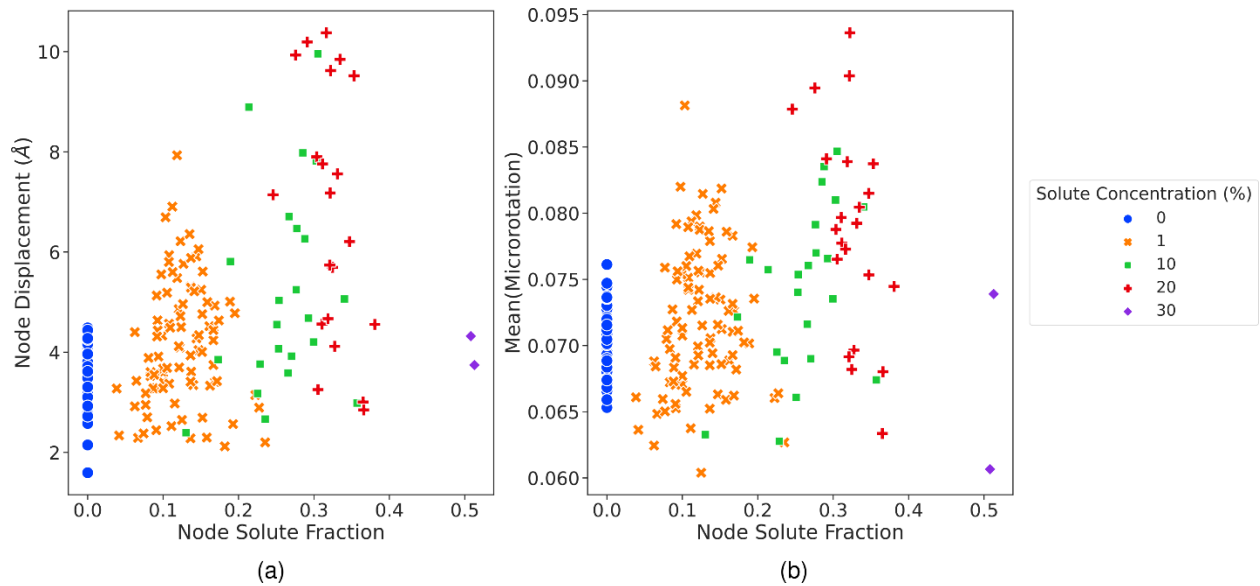
Figure 13: Plots of node displacement versus solute concentration and mean node microrotation versus solute fraction for atoms which undergo structure change due to the glide of misfit nodes. No clear relationship between solute fraction and either misfit node displacement or average microrotation is observed. This indicates that misfit node glide is not a localized event and is instead dependent on the longer-range configuration formed by the misfit pattern and solutes.

Focus to this point has been placed on quantifying misfit node glide and the associated deformation; however, glide of misfit dislocations is also expected to occur. To quantify and compare the deformation of misfit dislocations and misfit nodes, average microrotation vector magnitudes are calculated in atomic neighborhoods surrounding points along the misfit dislocation lines and the misfit nodes. Analysis of the evolution of misfit dislocation points in a manner similar to the previously presented misfit node analysis is made difficult by the inaccuracy associated with determining exact positions along the misfit dislocation line when using DXA. This is particularly true closer to the highly distorted misfit node regions. Extraction of positions along the misfit dislocation line using excess volume analysis is also not feasible due to large fluctuations in the excess volume associated with solute atoms. Analysis of the microrotation vector magnitudes near misfit dislocation lines extracted via DXA provides insight into the degree of misfit dislocation glide without requiring rigorous tracking of points along the misfit dislocation lines. These atomic neighborhoods are calculated using the same methodology as used to calculate the solute fractions in Fig. 6. The distribution of averaged microrotation vector magnitudes over several strain increments are then rendered as box plots and shown in Fig. 12. The distribution of average microrotation vector magnitudes shows that misfit nodes are the primary sites of interface structure deformation, while misfit dislocations are secondary sites. As expected, both are higher than the interface average. This trend matches the expected deformation pathway of Cu/Ni semi-coherent interfaces, which has been shown to initiate at misfit nodes and then progress along the misfit dislocation lines [39]. An increase in the spread of values accompanies the increase in solute concentration, reflecting the heterogenous misfit node sliding as discussed previously. It is important to

note that the present analysis includes the mean microrotation vector magnitude for all misfit nodes regardless of whether they have undergone glide or not. Lower mean microrotation vector magnitudes can be attributed to misfit nodes or misfit dislocations that have undergone no glide. Increase in the spread of microrotation vector magnitudes means both larger and smaller, or non-existent, node displacements which often occur for the same strain increment. This suggests heterogeneous misfit node and misfit dislocation glide which may occur as a result of heterogeneous interface resistance to sliding. The increase in maximum mean microrotation vector magnitude can be attributed to both larger node displacements and more complex restructuring at the misfit node as previously discussed. Maximum microrotation vector magnitudes for atoms near misfit dislocations increases alongside the increase in misfit node microrotations. The 0% and 1% models exhibit very similar microrotation distributions for atoms near misfit dislocations. Further increases to the solute fraction lead to increasing microrotation for atoms near misfit dislocations with the 20% solute concentration model exhibiting the largest values. This analysis reveals a transition from primarily misfit node glide to a combination of misfit dislocation and misfit node glide with increasing solute concentration.
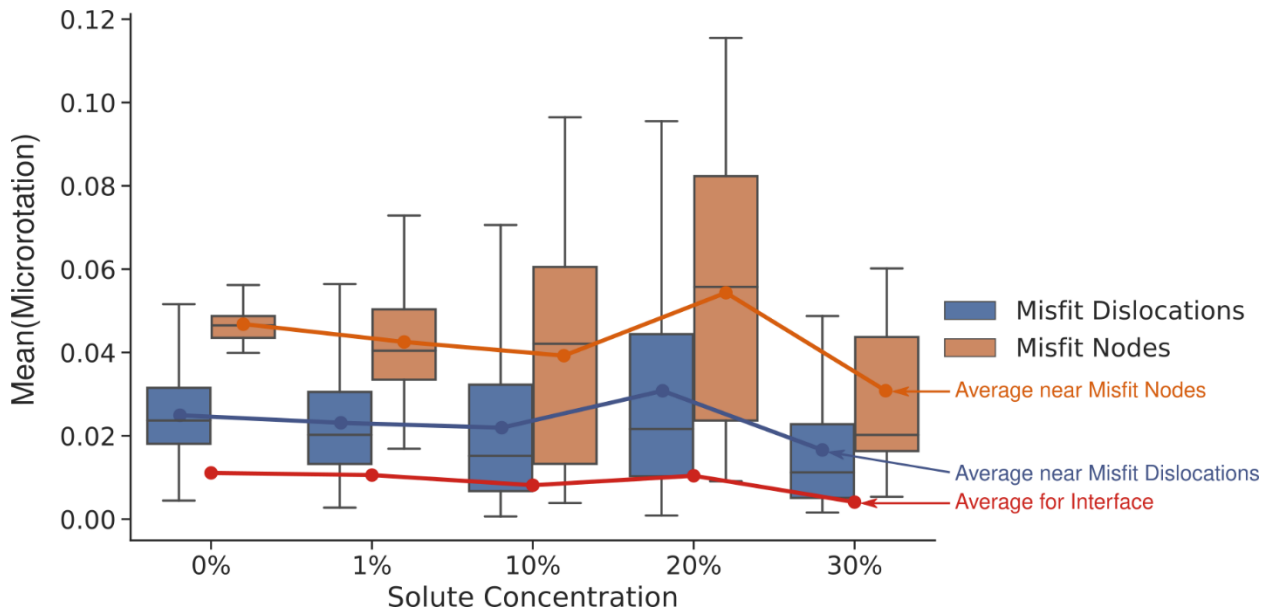

Figure 14: Box plots depicting distribution of microrotation magnitude for atoms within a spherical shell of 1.5 nm near misfit dislocations and misfit dislocation nodes averaged over several strain steps. Line plots mark average values with red denoting the overall interface average value. As expected, atoms near misfit nodes exhibit the highest degree of restructuring as determined by the microrotation magnitude. Increased solute concentration increases both the spread of microrotation values and the maximum values observed but does not change the average significantly. Increased spread in observed values implies increased spread in the local resistance to misfit dislocation glide.

3.5. Qualitative comparisons of energy barriers for interface sliding

The microrotation filtering employed in previous sections to characterize the distribution of deformation along the interface can also be used to compute approximate energy

barriers for interface sliding for comparing the investigated geometries. It is noted that the methodology used to compute the change in energy should not be regarded as a quantitative estimate of the activation energy barrier for the process (such as that calculated by NEB methods [73]) but rather as a means to enable qualitative comparisons of the interface energetics of misfit dislocation glide between the various interface structures investigated. A methodology similar to the one used to calculate node displacements in Fig. 8 is applied to calculate the change curves plotted in Fig. 13 for change of energy per node. Simulation snapshots of all geometries at three different applied shear strains are analyzed, corresponding to three different points on the stress-strain curves in Fig 7a). The microrotation vector is calculated using the atomic positions corresponding to the selected shear strain, e.g., 0.0425, and the atomic positions at a lower shear strain separated by an increment of $2.5x10^{-4}$, e.g., 0.0400. Atoms are then filtered by microrotation using a cutoff of 0.06 as in previous analysis. The change in energy plot using $4.75x10^{-3}$ shear strain as the current configuration for the microrotation vector analysis corresponds to the first shear stress maxima in Fig. 7. Atoms are grouped to the nearest node by minimum Euclidian norm between the atom position and the misfit node centroid and summed to produce a total change in energy associated with that node. The average change in energy per node is then plotted in Fig. 13. The three different changes in energy plots in Fig. 13 correspond to three distinct evolutions of the misfit dislocation pattern through misfit dislocation and misfit node glide. These are distinct in that the starting configuration and ending configuration of the misfit pattern is unique to each. The methodology used here closely resembles the control box method presented by Sangid et al. [74].
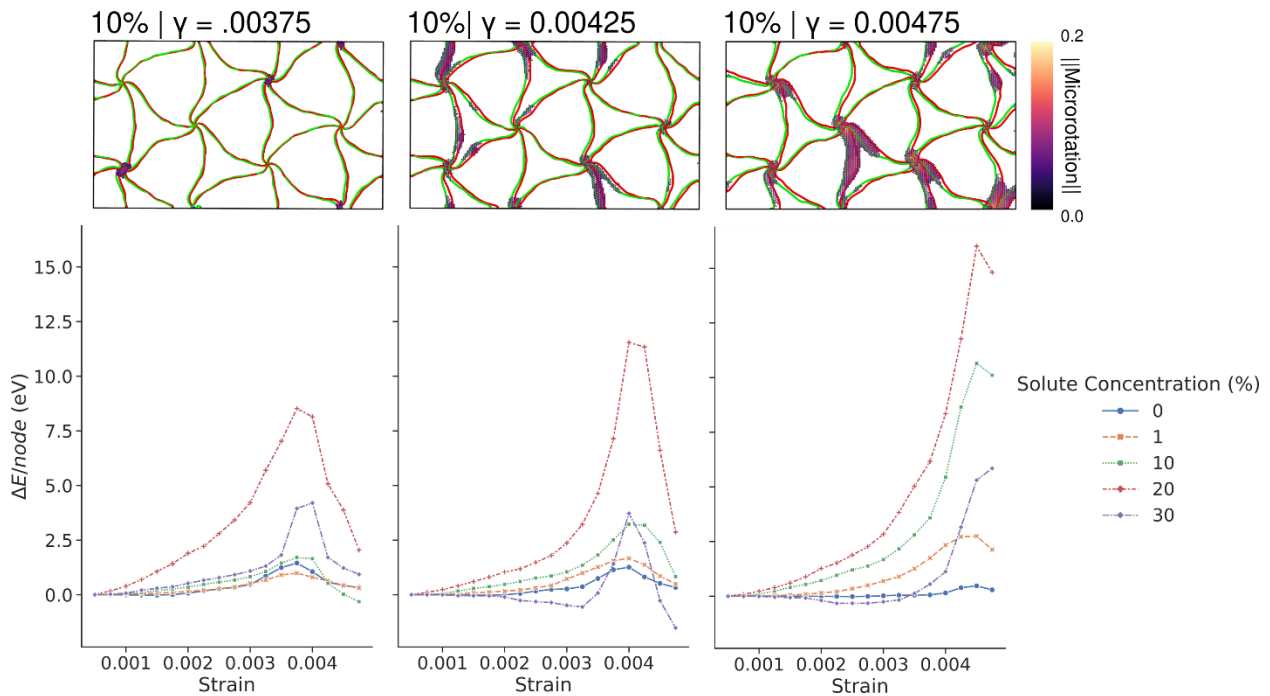

Figure 15: Calculated change in energy per node for associated atoms that have undergone node deformation as a result of the evolution of the misfit dislocation pattern for different starting configurations. Each change in energy plot approximates the energy barrier for sliding. The inset images show the atoms which have participated in the misfit pattern

deformation and used to calculate the change in energy plots for the 10% solute concentration. In the inset images, green dislocation lines representing dislocations in the reference configuration and the red dislocation lines representing dislocations in the current configuration.

As the misfit dislocation pattern glides across the interface, it encounters a complex energy landscape. In the case of heterogenous solute distribution at the interface, the dislocation network is pinned in local energy minima. These energy minima are not uniform for the entire misfit pattern. The previous analysis showing heterogenous node displacements suggest distributed glide resistance. Application of shear stress allows the misfit pattern to overcome smaller energy barriers first, resulting in localized misfit node or misfit dislocation glide. The maximum stress in Fig 7 therefore corresponds to a misfit pattern configuration with the highest energy barrier for glide. This is confirmed by the present analysis as the maximum change in energy increases for misfit node glide at strains closer to the maximum peak stress. This energy analysis again suggests the efficacy of statistically distributed shear strengths in reduced order models to represent the fluctuation of energy barriers for interface sliding of misfit dislocations. The trend for maximum change in energy versus solute concentration for the 0%, 1%, 10%, and 30% solute concentration models are similar to that of the interface shear strength. The 20% model, however, has the largest maximum change in energy and the lowest shear strength among models with solutes at the interface. The cause for this behavior may arise from the previous finding that the 20% solute concentration model exhibits the highest degree of atomic deformation near misfit dislocations. Misfit dislocation glide is observed to be less prevalent in both the 0%, 1%, and 10% models, as shown numerically through the analysis of microrotation vector magnitudes for atoms near misfit dislocation lines in Fig. 12. This can also be observed qualitatively from a selection of representative model snapshots with atoms filtered by the microrotation shown in Fig. 14. Atoms which participate in misfit dislocation glide contribute additional energy and inflate the computed changes in energy per node for the 20% and 30% models. It is unclear, however, whether resistance to misfit dislocation glide contributes significantly to the energy barrier for interface sliding or whether the deformation pathway is dominated by the energy barrier for misfit node glide. The shear stress-strain response indicates that the larger change in energy per node for the 20% does not correlate with improved shear strength as expected. Separating the change in energies for solely misfit dislocation glide and misfit node glide is necessary to provide insight into the dominant deformation mechanism.
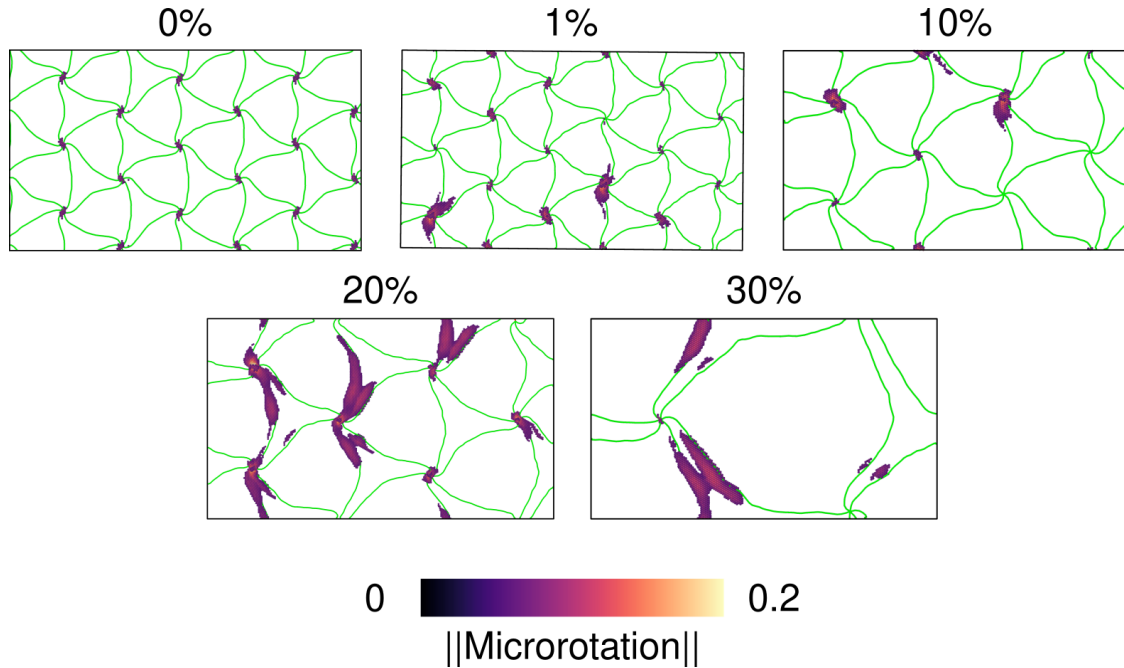
Figure 16: Representative simulation snapshots for all solute concentrations with atoms filtered by microrotation. It is observed that the 0%, 1%, and 10% model geometries exhibit primarily misfit node glide while the 30% exhibits significant misfit dislocation glide separate from any motion of the misfit node. The 20% model exhibits both misfit node glide and misfit dislocation glide which may contribute to the larger energies observed in Fig. 13.

It is necessary to distinguish atoms which participate in misfit dislocation glide from those that participate in misfit node glide to calculate associated energy change for each mechanism. The previous microrotation filtering technique combined with a K-Means clustering algorithm is applied to isolate atoms which belong to either the misfit node or the misfit dislocation. The number of clusters are selected by maximum silhouette score. This score measures the effectiveness of clustering algorithms by comparing intercluster distance and intracluster distance, i.e., the compactness of each cluster and the separation of the cluster centroids. This metric is commonly used to evaluate clustering algorithms [75]. Clusters corresponding to misfit node regions and misfit dislocation regions are manually selected from the inspected snapshot. The energies of those subsets of atoms can be tracked to generate similar change in energy curves for atoms involved in misfit dislocation glide and for those involved in misfit node glide. Results here are presented in terms of per-atom energy changes meaning that the difference in energies between atoms in their current state and their reference state are averaged for misfit dislocation glide atoms or misfit node glide atoms. The results of this analysis are presented in Fig. 15, with shaded regions denoting the 95% confidence interval. The misfit node has a higher change in energy than the glide of misfit dislocations for both 20% and 30% solute concentration models. This is the case even when segments of the misfit dislocation line glide seemingly independently from the misfit node, such as for the 30% snapshot investigated. The low change in energy per atom for misfit dislocation glide can be understood to result from the facilitation of misfit dislocation glide by the misfit node glide. Previously presented results show that misfit nodes are the primary sites of interface sliding, yet the lower change in

energy per atom for misfit dislocation glide suggest that misfit dislocation glide should occur more readily. This seeming contradiction can be resolved by understanding that the misfit dislocation glide is coupled to the misfit node glide. As a result, the lower change in atomic energy for misfit dislocation glide means that misfit dislocation glide is not significantly resisted, and instead the glide of misfit nodes controls the misfit pattern deformation, i.e., the rate-limiting step in the process.
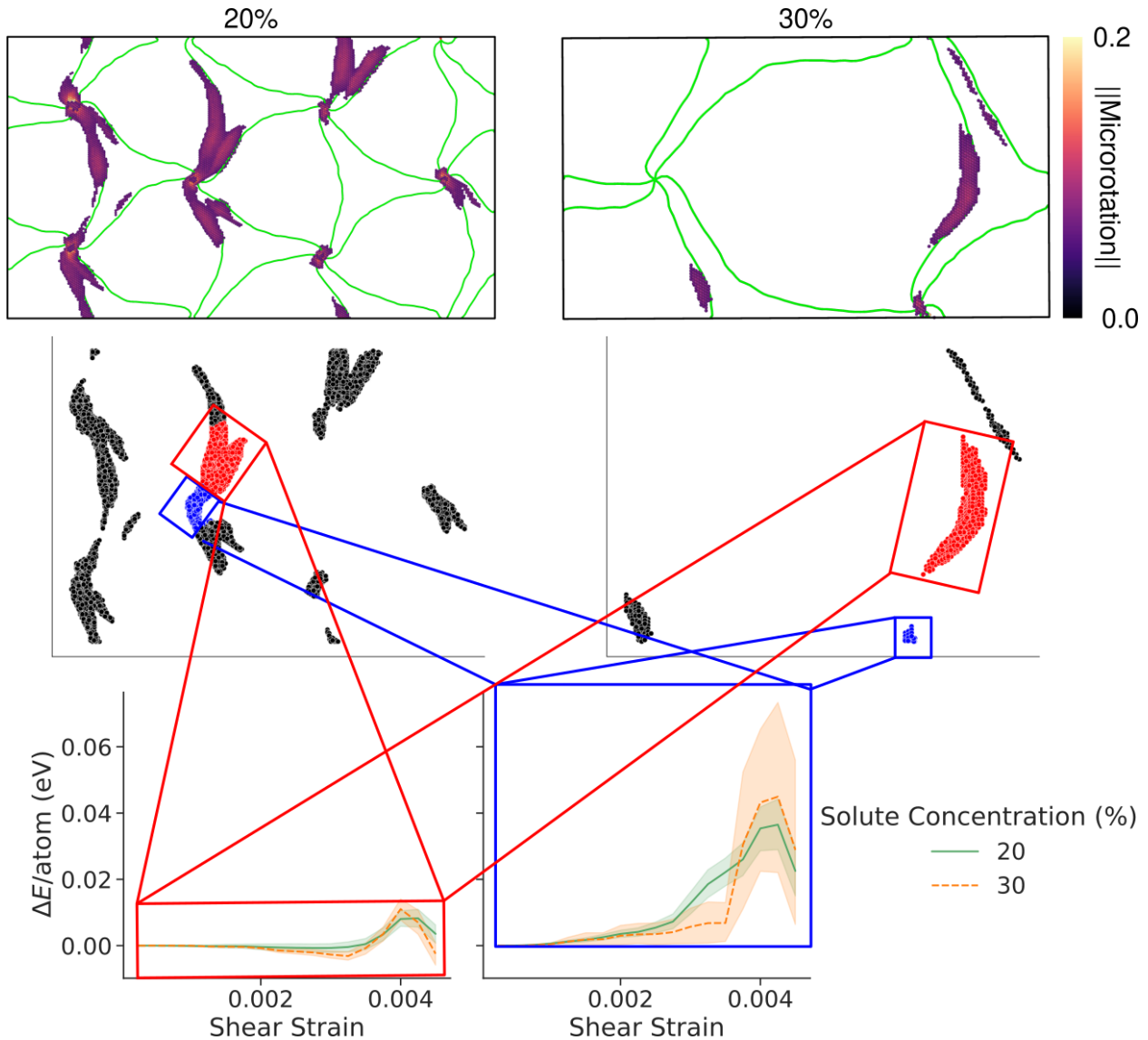

Figure 17: Atoms filtered by microrotation are grouped into atoms which have deformed as a result of either misfit dislocation glide (red) or misfit node glide (blue) with black denoting atoms not included in the calculation. Change in energy per atom plots are calculated for atoms which have deformed as a result of misfit dislocation glide (red box) or misfit node glide (blue box) for both solute concentrations.. When only atoms near misfit nodes are included in the calculation, a lower maximum energy change is observed for the 20%, suggesting a reduced barrier for misfit node glide compared to the 30% which is opposite of

the trend observed in Fig. 13. Here the shaded regions in the change in energy per atom plots represent the 95% confidence interval.

In Fig. 13. the 20% solute concentration model has a higher average change in energy per node than the 30% model, yet when only atoms near misfit nodes are included, this trend is reversed, and the 20% solute concentration model is revealed to have a lower change in energy as observed in Fig. 15. This matches the trend for shear strength in Fig. 7. It is observed through comparison of both Fig. 13 and Fig 15 that increasing solute concentration generally increases the change in atomic energy per node, indicating that a higher energy barrier for misfit node glide is associated with increased solute concentrations. This trend is not monotonic, however, as the 20% solute concentration model has a lower maximum change in energy than the 30% solute concentration model when only atoms participating in misfit node glide are included. The distribution of energy barrier strengths is confirmed by the differences in the change in atomic energy per node when different misfit configurations are considered. Determination of structure factors which lead to improved interface resistance to sliding will be important for improved design of nanolaminate interfaces and is left for future work.

4. Conclusions

In summary, interdiffusion is an important consideration when modeling metallic nanolaminates with semi-coherent interfaces as it can affect misfit dislocation interface glide mechanisms and resulting shear strength. When considering interdiffusion, it is important to consider both the addition of solute atoms and the scaling of the layer lattice constant by the solute concentration, along with concentration gradients near the interface and segregation at misfit dislocations. The primary findings of this work are as follows:

- Solute atoms in the Ni/Cu system segregate to both misfit dislocations and misfit nodes. Solute clustering is not observed and instead solutes tend to order themselves randomly.
- Interface shear strength increases with solute concentration; however, this increase is not monotonic due to the competing effects of solute-dislocation strengthening and decreased misfit density in reducing resistance to sliding. Fluctuations in the shear strength for models with solutes indicate a distribution of misfit-solute configurations which lead to a distribution of resistance to glide of misfit dislocation nodes.
- Addition of solutes causes a switch from uniform interface sliding to heterogeneous interface sliding where only select misfit nodes/dislocations glide due to a distribution of local energetic barriers. The solute environment directly surrounding a misfit node is not strongly correlated with the initial node deformation.
- Rough estimates for the energetic barriers to energy pathways resulting from interface sliding were computed; these correlated well with shear strength. Increased solute concentration is correlated with increased maximum energy along the energy pathway for atoms deformed by the glide of the interface misfit pattern; however, this correlation is not monotonic and further work is necessary to

determine the structure factors which contribute to larger energy barriers in the distribution.

- Misfit dislocation glide was found to occur readily alongside misfit node glide, as evaluated by the low change in atomic energy per atom for misfit dislocation glide. Interface sliding depends primarily on misfit node glide. Misfit node response to shear may therefore be the primary consideration for accurate modeling of nanolaminate response to shear loading.
- The microrotation is found to be a useful metric which can quantify various aspects of the interface deformation and enables the detailed relative energy barrier estimates conducted for misfit dislocation glide.

The results highlight the importance of modeling more realistic diffuse interface structures for predicting nanolaminate properties. A methodology is presented that employs the microrotation metric for to estimate energy barriers during interface sliding/restructuring. The competing roles of misfit dislocation density and solute concentration require further investigation through targeted simulations that isolate each parameter to the extent possible. Extension of present work to larger scales through the use of the Concurrent Atomistic-Continuum method [76-79] can provide additional insight into the deformation behavior of nanolaminate materials by modeling larger interface spacings and period cell sizes. Further study of experimental process conditions to control diffuse interface structure and resulting properties is desirable to foster interplay of these simulations with experiments regarding interface behavior to demonstrate the efficacy of this additional diffuse interface degree-of-freedom in tailoring nanolaminates for specific applications or property targets.

5. Acknowledgements

6. References

[1] S. Huang and C. Zhou, Fracture resistance of Cu/Nb metallic nanolayered composite, Journal of Materials Research, 34 (2019) 1533-1541.

[2] R. Gao, M. Jin, F. Han, B. Wang, X. Wang, Q. Fang, Y. Dong, C. Sun, L. Shao, M. Li, J. Li, Superconducting Cu/Nb nanolaminate by coded accumulative roll bonding and its helium damage characteristics, Acta Materialia, 197 (2020) 212-223.

[3] A. A. Minakov., A. I. Plokhikh, A. Schmiedt, and F. Walther, Comparative analysis of the fatigue characteristics of multilayer steel materials and nanolaminates, AIP Conference Proceedings. 2053 (2018) 040059 .

[4] M. Nasim, Y. Li, M. Dargusch, and C. Wen, Ultra-strong and ductile Ta/Co nanolaminates strengthened via grain-boundary expanding and interfacial sliding, Applied Materials Today. 23 (2021) 100983.

[5] A. Sáenz-Trevizo, A.M. Hodge, Nanomaterials by design: A review of nanoscale metallic multilayers, Nanotechnology. 31 (2020) 292002. https://doi.org/10.1088/1361-6528/ab803f.

[6] Q. Zhou, J.Y. Xie, F. Wang, P. Huang, K.W. Xu, T.J. Lu, The mechanical behavior of nanoscale metallic multilayers: A survey, Acta Mechanica Sinica. 31 (2015) 319–337. https://doi.org/10.1007/s10409-015-0401-1.

[7] W. R. Jian, S. Xu, Y. Su, and I. J. Beyerlein, Role of layer thickness and dislocation distribution in confined layer slip in nanolaminated Nb, International Journal of Plasticity, 152 (2022) 103239.

[8] Z.H. Cao, Y.P. Cai, C. Sun, Y.J. Ma, M.Z. Wei, Q. Li, H.M. Lu, H. Wang, X. Zhang, X.K. Meng, Tailoring strength and plasticity of Ag/Nb nanolaminates via intrinsic microstructure and extrinsic dimension, International Journal of Plasticity. 113 (2019) 145–157. https://doi.org/10.1016/j.ijplas.2018.09.012.

[9] J. Snel, M.A. Monclús, M. Castillo-Rodríguez, N. Mara, I.J. Beyerlein, J. Llorca, J.M. Molina-Aldareguía, Deformation mechanism map of Cu/Nb nanoscale metallic multilayers as a function of temperature and layer thickness, JOM. 69 (2017) 2214–2226. https://doi.org/10.1007/s11837-017-2533-1.

[10] M. Nasim, Y. Li, and C. Wen, Length-scale dependent deformation, strengthening, and ductility of fcc/fcc Ni/Al nanolaminates using micropillar compression testing, Acta Materialia 193 (2020) 318-328.,

[11] J.S. Carpenter, A. Misra, P.M. Anderson, Achieving maximum hardness in semi-coherent multilayer thin films with unequal layer thickness, Acta Materialia. 60 (2012) 2625–2636. https://doi.org/10.1016/j.actamat.2012.01.029.

[12] B. Zhang, Y. Kou, Y.Y. Xia, X. Zhang, Modulation of strength and plasticity of multiscale Ni/Cu laminated composites, Materials Science and Engineering: A. 636 (2015) 216–220. https://doi.org/10.1016/J.MSEA.2015.03.075.

[13] J.Y. Zhang, K. Wu, L.Y. Zhang, Y.Q. Wang, G. Liu, J. Sun, Unraveling the correlation between hall-petch slope and peak hardness in metallic nanolaminates, International Journal of Plasticity. 96 (2017) 120–134. https://doi.org/10.1016/j.ijplas.2017.04.020.

[14] M.R. An, H.Y. Song, Q. Deng, M.J. Su, Y.M. Liu, Influence of interface with mismatch dislocations on mechanical properties of Ti/Al nanolaminate, Journal of Applied Physics. 125 (2019) 165307. https://doi.org/10.1063/1.5085455.

[15] H. Yang, L. Zhu, R. Zhang, J. Zhou, Z. Sun, Shearing dominated by the coupling of the interfacial misfit and atomic bonding at the FCC (111) semi-coherent interfaces, Materials & Design. 186 (2020) 108294. https://doi.org/10.1016/j.matdes.2019.108294.

[16] R.F. Zhang, T.C. Germann, J. Wang, X.-Y. Liu, I.J. Beyerlein, Role of interface structure on the plastic response of Cu/Nb nanolaminates under shock compression: Non-equilibrium molecular dynamics simulations, Scripta Materialia. 68 (2013) 114–117. https://doi.org/10.1016/j.scriptamat.2012.09.022.

[17] J. Wang, R.F. Zhang, C.Z. Zhou, I.J. Beyerlein, A. Misra, Interface dislocation patterns and dislocation nucleation in face-centered-cubic and body-centered-cubic bicrystal interfaces, 53 (2014) 40–55. https://doi.org/10.1016/j.ijplas.2013.07.002.

[18] M. Xiang, Y. Liao, K. Wang, G. Lu, J. Chen, Shock-induced plasticity in semi-coherent {111} Cu-Ni multilayers, International Journal of Plasticity. 103 (2018) 23–38. https://doi.org/10.1016/j.ijplas.2017.12.005.

[19] A. Hunter, B. Leu, I. J. Beyerlein, A review of slip transfer: applications of mesoscale techniques, Journal of Materials Science. 53 (2018) 5584-5603.

[20] X. Tian, J. Cui, M. Yang, K. Ma, M. Xiang, Molecular dynamics simulations on shock response and spalling behaviors of semi-coherent {111} Cu-Al multilayers, International Journal of Mechanical Sciences. 172 (2020) 105414.

[21] Y. Li, Q. Zhou, S. Zhang, P. Huang, K. Xu, F. Wang, T. Lu, On the role of weak interface in crack blunting process in nanoscale layered composites, Applied Surface Science. 433 (2018) 957–962. https://doi.org/10.1016/j.apsusc.2017.10.002.

[22] Q. Zhou, Y. Ren, Y. Du, D. Hua, W. Han, Cracking and toughening mechanisms in nanoscale metallic multilayer films: A brief review, Applied Sciences. 8 (2018) 1821. https://doi.org/10.3390/app8101821.

[23] C. Lv, J. Yang, X. Zhang, Y. Cai, X. Liu, G. Wang, S.-N. Luo, Interfacial effect on deformation and failure of Al/Cu nanolaminates under shear loading, Journal of Physics D: Applied Physics. 51 (2018) 335301.

[24] T. Fu, X. Peng, X. Chen, S. Weng, N. Hu, Q. Li, Z. Wang, Molecular dynamics simulation of nanoindentation on Cu/Ni nanotwinned multilayer films using a spherical indenter, Scientific Reports. 6 (2016) 35665. https://doi.org/10.1038/srep35665.

[25] F. Yin, Y. Zhao, S. Yu, W. Pang, Molecular dynamics studies on the interface evolution characteristics and deformation mechanisms of Cu/Al multilayers during compression process, Journal of Applied Physics. 125 (2019) 025112. https://doi.org/10.1063/1.5055901.

[26] S. Shao, H.M. Zbib, I. Mastorakos, D.F. Bahr, Effect of interfaces in the work hardening of nanoscale multilayer metallic composites during nanoindentation: A molecular dynamics investigation, Journal of Engineering Materials and Technology. 135 (2013). https://doi.org/10.1115/1.4023672.

[27] A.V. Druzhinin, B. Rheingans, S. Siol, B. B. Straumal, J. Janczak-Rusch, L. P. Jeurgens, C. Cancellieri, Effect of internal stress on short-circuit diffusion in thin films and nanolaminates, Applied Surface Science. 508 (2020), 145254

[28] Y. Sun, Y. Chen, N. Tsuji, S. Guan, Microstructural evolution and mechanical properties of nanostructured Cu/Ni multilayer fabricated by accumulative roll bonding, Journal of Alloys and Compounds. 819 (2020) 152956. https://doi.org/10.1016/j.jallcom.2019.152956.

[29] L.F. Zhang, R. Gao, B.L. Zhao, M. Sun, K. Jing, X.P. Wang, T. Hao, Z.M. Xie, R. Liu, Q.F. Fang, C.S. Liu, Effects of annealing temperature and layer thickness on hardening behavior in cross accumulative roll bonded Cu/Fe nanolamellar composite, Journal of Alloys and Compounds. 827 (2020) 154312. https://doi.org/10.1016/j.jallcom.2020.154312.

[30] M. Nasim, Y. Li, C. Wen, Individual layer thickness-dependent microstructures and mechanical properties of fcc/fcc Ni/Al nanolaminates and their strengthening mechanisms, Materialia. 6 (2019) 100347. https://doi.org/10.1016/j.mtla.2019.100347.

[31] J.M. Roussel, P. Bellon, Interface sharpening and broadening during annealing of Cu/Ni multilayers: A kinetic Monte Carlo study, Physical Review B. 73 (2006) 085403

[32] X.L. Yan, Y. Liu, H.C. Swart, J.Y. Wang, J.J. Terblans, Investigation of interdiffusion and depth resolution in Cu/Ni multilayers by means of AES depth profiling, Applied Surface Science. 364 (2016) 567–572. https://doi.org/10.1016/j.apsusc.2015.12.151.

[33] W. R. Jian, Y. Su, S. Xu, W. Ji, I. J. Beyerlein, Effect of interface structure on dislocation glide behavior in nanolaminates, Journal of Materials Research. 36 (2021) 2802-2815.

[34] S.I. Rao, P.M. Hazzledine, Atomistic simulations of dislocation–interface interactions in the Cu-Ni multilayer system, Philosophical Magazine A. 80 (2000) 2011–2040. https://doi.org/10.1080/01418610008212148.

[35] R. Dikken, M. Khajeh Salehani, Edge dislocation impingement on interfaces between dissimilar metals, (2017). https://hal.archives-ouvertes.fr/hal-01572509.

[36] S. Xu, Y. Li, Y. Chen, Si/Ge (111) semicoherent interfaces: Responses to an in-plane shear and interactions with lattice dislocations, Physica Status Solidi (b). 257 (2020) 2000274. https://doi.org/10.1002/pssb.202000274.

[37] S. Shao, J. Wang, I.J. Beyerlein, A. Misra, Glide dislocation nucleation from dislocation nodes at semi-coherent { 1 1 1 } Cu-Ni interfaces, Acta Materialia. 98 (2015) 206–220. https://doi.org/10.1016/j.actamat.2015.07.044.

[38] A. Selimov, S. Xu, Y. Chen, D. McDowell, Lattice dislocation induced misfit dislocation evolution in semi-coherent 111 bimetal interfaces, Journal of Materials Research. (2021). https://doi.org/10.1557\%2Fs43578-021-00184-8.

[39] X.Y. Chen, X.F. Kong, A. Misra, D. Legut, B.N. Yao, T.C. Germann, R.F. Zhang, Effect of dynamic evolution of misfit dislocation pattern on dislocation nucleation and shear sliding at semi-coherent bimetal interfaces, Acta Materialia. 143 (2018) 107–120. https://doi.org/10.1016/j.actamat.2017.10.012.

[40] F. Moszner, C. Cancellieri, M. Chiodi, S. Yoon, D. Ariosa, J. Janczak-Rusch, L.P.H. Jeurgens, Thermal stability of Cu/W nano-multilayers, Acta Materialia. 107 (2016) 345–353. https://doi.org/10.1016/j.actamat.2016.02.003.

[41] M. Chládek, C. Dorner, A. Buchal, V. Valvoda, H. Hoffmann, Quantitative in situ x-ray diffraction analysis of magnetic multilayers during annealing, Journal of Applied Physics. 80 (1996) 1437–1445. https://doi.org/10.1063/1.363011.

[42] H. Aboulfadl, F. Seifried, M. Stueber, F. Muecklich, Interdiffusion in as-deposited Ni/Ti multilayer thin films analyzed by atom probe tomography, Materials Letters. 236 (2019) 92-95.

[43] S. Shao, J. Wang, A. Misra, Energy minimization mechanisms of semi-coherent interfaces, Journal of Applied Physics. 116 (2014) 023508.

[44] C.J. Wang, B.N. Yao, Z.R. Liu, X.F. Kong, D. Legut, R.F. Zhang, Y. Deng, Effects of solutes on dislocation nucleation and interface sliding of bimetal semi-coherent interface, International Journal of Plasticity. 131 (2020) 102725. https://doi.org/10.1016/j.ijplas.2020.102725.

[45] M.I. Pascuet, G. Monnet, G. Bonny, E. Martínez, J.J.H. Lim, M.G. Burke, L. Malerba, Solute precipitation on a screw dislocation and its effects on dislocation mobility in bcc Fe, Journal of Nuclear Materials. 519 (2019) 265–273. https://doi.org/10.1016/j.jnucmat.2019.04.007.

[46] C. Varvenne, G.P.M. Leyson, M. Ghazisaeidi, W.A. Curtin, Solute strengthening in random alloys, Acta Materialia. 124 (2017) 660–683. https://doi.org/10.1016/j.actamat.2016.09.046.

[47] I.A. Bryukhanov, Dynamics of edge dislocation in Cu–Ni solid solution alloys at atomic scale, International Journal of Plasticity. 135 (2020) 102834. https://doi.org/10.1016/j.ijplas.2020.102834.

[48] W.G. Nöhring, W.A. Curtin, Dislocation cross-slip in fcc solid solution alloys, Acta Materialia. 128 (2017) 135–148. https://doi.org/10.1016/j.actamat.2017.02.027.

[49] A. Gola, P. Gumbsch, L. Pastewka, Atomic-scale simulation of structure and mechanical properties of $Cu_{1-x}Ag_x$|Ni multilayer systems, Acta Materialia. 150 (2018) 236–247. https://doi.org/10.1016/j.actamat.2018.02.046.

[50] A. Gola, L. Pastewka, K. Binder, M. Müller, A. Trautmann, Structure of interfaces in Cu| Au nanolaminates, in: NIC Symposium, 2018: pp. 247–254.

[51] J. Y. Cheng, S. Xu, Y. Chen, Z. Li, J. K. Baldwin, I. J. Beyerlein, and N. A. Mara, Simultaneous High-Strength and Deformable Nanolaminates With Thick Biphase Interfaces, Nano letters. 22 (2022). 1897-1904.

[52] Y. Chen, N. Li, R. G. Hoagland, X-Y. Liu, J. K. Baldwin, I. J. Beyerlein, J. Y. Cheng, and N. A. Mara, Effects of three-dimensional Cu/Nb interfaces on strengthening and shear banding in nanoscale metallic multilayers, Acta Materialia. 199 (2020). 593-601.

[53] A. Stukowski, K. Albe, Dislocation detection algorithm for atomistic simulations, Modelling and Simulation in Materials Science and Engineering. 18 (2010) 025016. https://doi.org/10.1088/0965-0393/18/2/025016.

[54] A.P. Thompson, H.M. Aktulga, R. Berger, D.S. Bolintineanu, W.M. Brown, P.S. Crozier, P.J. in 't. Veld, A. Kohlmeyer, S.G. Moore, T.D. Nguyen, R. Shan, M.J. Stevens, J. Tranchida, C. Trott, S.J. Plimpton, LAMMPS - a flexible simulation tool for particle-based materials modeling at the atomic, meso, and continuum scales, Computer Physics Communications. 271 (2022) 108171. https://doi.org/10.1016/j.cpc.2021.108171.

[55] J. Guénolé, W. G. Nöhring, A. Vaid, F. Houllé, Z. Xie, A. Prakash, and E. Bitzek, Assessment and optimization of the fast inertial relaxation engine (fire) for energy minimization in atomistic simulations and its implementation in lammps, Computational Materials Science. 175 (2020) 109584.

[56] M. Parrinello, A. Rahman, Polymorphic transitions in single crystals: A new molecular dynamics method, Journal of Applied Physics. 52 (1981) 7182–7190. https://doi.org/10.1063/1.328693.

[57] B. Onat, S. Durukanoğlu, An optimized interatomic potential for Cu-Ni alloys with the embedded-atom method, Journal of Physics Condensed Matter. 26 (2014).

[58] A. Stukowski, Visualization and analysis of atomistic simulation data with OVITO–the open visualization tool, Modelling and Simulation in Materials Science and Engineering. 18 (2009) 015012. https://doi.org/10.1088/0965-0393/18/1/015012.

[59] M. Zhou, A new look at the atomic level virial stress: On continuum-molecular system equivalence, Proceedings of the Royal Society of London. Series A: Mathematical, Physical and Engineering Sciences. 459 (2003) 2347–2392. https://doi.org/10.1098/rspa.2003.1127.

[60] W.-R. Jian, S. Xu, I.J. Beyerlein, On the significance of model design in atomistic calculations of the peierls stress in Nb, Computational Materials Science. 188 (2021) 110150. https://doi.org/10.1016/j.commatsci.2020.110150.

[61] J.D. Honeycutt, H.C. Andersen, Molecular dynamics study of melting and freezing of small Lennard-Jones clusters, Journal of Physical Chemistry. 91 (1987) 4950–4963.

[62] G.J. Tucker, J.A. Zimmerman, D.L. McDowell, Shear deformation kinematics of bicrystalline grain boundaries in atomistic simulations, Modelling and Simulation in Materials Science and Engineering. 18 (2009) 015002. https://doi.org/10.1088/0965-0393/18/1/015002.

[63] G.J. Tucker, J.A. Zimmerman, D.L. McDowell, Continuum metrics for deformation and microrotation from atomistic simulations: Application to grain boundaries, International Journal of Engineering Science. 49 (2011) 1424–1434. https://doi.org/10.1016/j.ijengsci.2011.03.019.

[64] F. Pedregosa, G. Varoquaux, A. Gramfort, V. Michel, B. Thirion, O. Grisel, M. Blondel, P. Prettenhofer, R. Weiss, V. Dubourg, J. Vanderplas, A. Passos, D. Cournapeau, M. Brucher, M. Perrot, E. Duchesnay, Scikit-learn: Machine learning in Python, Journal of Machine Learning Research. 12 (2011) 2825–2830.

[65] P. Virtanen, R. Gommers, T.E. Oliphant, M. Haberland, T. Reddy, D. Cournapeau, E. Burovski, P. Peterson, W. Weckesser, J. Bright, S.J. van der Walt, M. Brett, J. Wilson, K.J. Millman, N. Mayorov, A.R.J. Nelson, E. Jones, R. Kern, E. Larson, C.J. Carey, ˙Ilhan. Polat, Y. Feng, E.W. Moore, J. VanderPlas, D. Laxalde, J. Perktold, R. Cimrman, I. Henriksen, E.A. Quintero, C.R. Harris, A.M. Archibald, A.H. Ribeiro, F. Pedregosa, P. van Mulbregt, A. Vijaykumar, A.P. Bardelli, A. Rothberg, A. Hilboll, A. Kloeckner, A. Scopatz, A. Lee, A. Rokem, C.N. Woods, C. Fulton, C. Masson, C. Häggström, C. Fitzgerald, D.A. Nicholson, D.R. Hagen, D.V. Pasechnik, E. Olivetti, E. Martin, E. Wieser, F. Silva, F. Lenders, F. Wilhelm, G. Young, G.A. Price, G.-L. Ingold, G.E. Allen, G.R. Lee, H. Audren, I. Probst, J.P. Dietrich, J. Silterra, J.T. Webber, J. Slavič, J. Nothman, J. Buchner, J. Kulick, J.L. Schönberger, J.V. de Miranda Cardoso, J. Reimer, J. Harrington, J.L.C. Rodríguez, J. Nunez-Iglesias, J. Kuczynski, K. Tritz, M. Thoma, M. Newville, M. Kümmerer, M. Bolingbroke, M. Tartre, M. Pak, N.J. Smith, N. Nowaczyk, N. Shebanov, O. Pavlyk, P.A. Brodtkorb, P. Lee, R.T. McGibbon, R. Feldbauer, S. Lewis, S. Tygier, S. Sievert, S. Vigna, S. Peterson, S. More, T. Pudlik, T. Oshima, T.J. Pingel, T.P. Robitaille, T. Spura, T.R. Jones, T. Cera, T. Leslie, T. Zito, T. Krauss, U. Upadhyay, Y.O. Halchenko, Y.V.-B. and, SciPy 1.0: Fundamental algorithms for scientific computing in python, Nature Methods. 17 (2020) 261–272. https://doi.org/10.1038/s41592-019-0686-2.

[66] S. Shao, J. Wang, A. Misra, R.G. Hoagland, Spiral patterns of dislocations at nodes in (111) semi-coherent FCC interfaces, Scientific Reports. 3 (2013). https://doi.org/10.1038\%2Fsrep02448.

[67] X. Zhang, B. Zhang, Y. Mu, S. Shao, C. D. Wick, B. R. Ramachandran, W. J. Meng, Mechanical failure of metal/ceramic interfacial regions under shear loading, Acta Materialia. 138 (2017) 224-236.

[68] M. Dodaran, J. Wang, Y. Chen, W. J. Meng, S. Shao, Energetic, structural and mechanical properties of terraced interfaces. Acta Materialia. 171 (2019) 92-107.

[69] Y. Yao, T. Wang, C. Wang, Peierls-Nabarro model of interfacial misfit dislocation: An analytic solution, Physical Review B. 59 (1999) 8232.

[70] Y. Mishin, Solute drag and dynamic phase transformations in moving grain boundaries, Acta Materialia. 179 (2019) 383–395. https://doi.org/10.1016/j.actamat.2019.08.046.

[71] D.L. Olmsted, L.G. HectorJr, W.A. Curtin, R.J. Clifton, Atomistic simulations of dislocation mobility in al, ni and al/mg alloys, Modelling and Simulation in Materials Science and Engineering. 13 (2005) 371–388. https://doi.org/10.1088/0965-0393/13/3/007.

[72] A.P. Bartók, R. Kondor, G. Csányi, On representing chemical environments, Physical Review B. 87 (2013). https://doi.org/10.1103/physrevb.87.184115.

[73] G. Henkelman, B.P. Uberuaga, H. Jónsson, A climbing image nudged elastic band method for finding saddle points and minimum energy paths, The Journal of Chemical Physics. 113 (2000) 9901–9904. https://doi.org/10.1063/1.1329672.

[74] M.D. Sangid, T. Ezaz, H. Sehitoglu, I.M. Robertson, Energy of slip transmission and nucleation at grain boundaries, Acta Materialia. 59 (2011) 283–296. https://doi.org/10.1016/j.actamat.2010.09.032.

[75] Shahapure, K. R., & Nicholas, C., Cluster quality analysis using silhouette score. 2020 IEEE 7th International Conference on Data Science and Advanced Analytics (DSAA) (2020) pp. 747-748

[76] Xu, S., Che, R., Xiong, L., Chen, Y. and McDowell, D.L., "A Quasistatic Implementation of the Concurrent Atomistic-Continuum Method for FCC Crystals, International Journal of Plasticity, Vol. 72, 2015, pp. 91-126.

[77] Xu, S., Xiong, L., Chen, Y. and McDowell, D.L., "Sequential slip transfer of mixed character dislocations across Σ3 coherent twin boundary in FCC metals: A concurrent atomistic-continuum study," npj Computational Materials 2, 15016, 2016, doi:10.1038/npjcompumats.2015.16.

[78] Chen, Y., Shabanov, S., and McDowell, D.L., "Concurrent Atomistic-Continuum Modeling

and Simulation of Crystalline Materials," Journal of Applied Physics, 126, 101101, 2019. https://doi.org/10.1063/1.5099653.

[79] Chu, K., Diaz, A., Chen, Y, Zhu, T., and McDowell, D.L., "Multiscale Concurrent Atomistic-Continuum (CAC) Modeling of Multicomponent Alloys," Computational Materials Science, Vol. 201, 2022, 110873.